Proposal of a hydrogen embrittlement index for a martensitic advanced high-strength steel

Francesco Aiello, Marco Beghini, Carlo Maria Belardini, Leonardo Bertini, Giuseppe Macoretta [*], Bernardo Disma Monelli [*], Renzo Valentini

Department of Civil and Industrial Engineering, University of Pisa, Largo Lucio Lazzarino 2, Pisa, 56122, Italy

ARTICLE INFO

ABSTRACT

This paper proposes a definition of a Hydrogen Embrittlement Index for assessing structural components made by a martensitic advanced high-strength steel. A material model, including a damage model and a fracture criterion, was developed to reproduce the tensile behaviour until fracture nucleation under different hydrogen concentrations. The analysis of the tests with different specimen geometries demonstrated that the maximum principal strain at fracture is correlated to hydrogen concentration, and it can be used to define the embrittlement index for quantifying the hydrogen susceptibility of material in a wide range of notch severity.

1. Introduction

Advanced High Strength Steels (AHSS) are widely used in the automotive industry [1–7]. Their high strength and ductility which guarantee crashworthiness and reduce the overall body weight of the car, thus contributing to greater passive safety and fewer polluting emissions [8–11]. Among AHSSs, Martensitic Steels (MS-AHSS) are used to produce automotive structural components that are crucial for impact safety, such as the front and rear bumper beams, door anti-intrusion bars, side sill reinforcements, and roof crossbars [12–14]. The success of MS-AHSS is a consequence of their strength and ductility, along with the relatively low cost [12,15]. However, due to their microstructure, MS-AHSS are particularly susceptible to Hydrogen Embrittlement (HE) [16].

H can be absorbed by steels either during the production processes, such as coating, welding, heat treatments, painting [17], or in particular service conditions [12]. The presence of Hydrogen (H) in steels can reduce strength, ductility, fatigue resistance, and fracture toughness [2, 12,17–21]. Two main distinct HE phenomena have been described in the literature: final fracture after a significant subcritical cracking or final fracture with no evidence of previous crack formation and stable growth (referred to as HESC and HEFT in [22]). The former case, which can be modelled with fracture mechanics approaches, is the most studied in the literature, whilst HE with no subcritical crack growth is generally associated with a reduction in ductility with no loss of strength [12,19,23–27]. Several mechanisms have been proposed to explain the embrittling effect of H, among others: (i) HEDE (ii) HELP (iii) HAM [21,22,24,28]. MS-AHSS components are usually manufactured by cold forming processes [12,29] in which significant plastic strains and strain gradients are generated and, consequently, intense residual stresses are present.

The residual stress and the dislocation density produced by cold forming processes can affect the diffusion of H and its distribution. In particular, H tends to accumulate in regions with tensile hydrostatic stress, where the local H concentration can become significantly larger than the mean value in the component [21,30]. As a consequence, even a small average concentration of H initially present in the material [12, 24] can accumulate and severely impair the component even in the absence of external loads, if there is sufficient time for H to diffuse and concentrate [17]. This process may explain the sudden cracking of steel components at some point after assembly or production, a phenomenon usually referred to as "delayed fracture" [31,32]. Delayed fractures have been observed by car component manufacturers at holes, fittings, and folds [33,34]. Delayed fracture tests require a long time and costly full-scale specimens, hence designers and steelmakers need preliminary data from small scale and faster tests on the HE susceptibility of materials.

Several tests have been proposed to perform this preliminary assessment of the susceptibility of AHSS to HE [16,17,33,35–42]. For this purpose, the Slow Strain Rate tensile Test (SSRT), performed under displacement control on a notched specimen, is the most widely used. The strain rate is kept low enough to allow H to migrate towards the notch tip region where the stress is at its peak. Due to H migration strain rate has an impact on the test results [38,43]. This test is particularly suitable for assessing the behaviour of sheet metal in the presence of

---

holes, whose boundaries are typical regions of crack initiation caused by HE in automotive components [33].

Two main approaches are commonly employed in the relevant literature: (i) H pre-charging and SSRT in air and (ii) SSRT in an H-inducing environment [26,44,45]. The first case is more adherent to the phenomenon of interest since usually cracking occurs without an hydrogenating environment, although it may require taking the H outgassing into consideration. Standard SEP1970 [41] defines a test specifically developed for assessing the strength properties of AHSS in the presence of H induced by the manufacturing processes.

A Hydrogen Embrittlement Index (HEI), measuring the change of a given property with H content, is commonly introduced to quantify the H deteriorating effect [46]. From the definition of the HEI, a critical H concentration [47] can be identified, which is defined as the threshold above which an unacceptable reduction in the chosen material property is expected, for example a 30% drop has been recommended [27].

Different methods to quantify and measure HE have been proposed, depending on the specific test and the mechanical property of interest [16,38,48–50]. Strength-, fracture toughness- or crack growth rate-based approaches are commonly used to evaluate the effects of H relevant for applications subjected to delayed fracture [43,45,51–54], or in the fields where a damage tolerant approach is needed. The HEI defined on the basis of quantities such as RA or elongation at fracture are technological properties, which not only depend on the material but also on the specimen used to calculate them. In particular, RA can be defined only on a uniformly stressed specimen, and the elongation at fracture changes its value when notched specimens are considered. As a consequence, the HEI defined with one of those methods is suitable for qualitative evaluations and comparisons between different materials, but it cannot generally be considered as a rational and effective measure of the material deterioration in the selected testing conditions. The aim of the present work is to propose a definition for the HEI that provides an estimation of the material deteriorating effect in the presence of notches. The study focuses on the MS-AHSS grade 1500, one of the most commonly used in the automotive industry. Several researchers have highlighted that, in MS-AHSSs, H provokes only a slight reduction in Yield Stress (YS) and Ultimate Tensile Strength (UTS), with a significant reduction in ductility [22,55–57]. Venezuela et al. have recently reported that the influence of H on notched specimens mostly occurs at the fracture nucleation region, and that no subcritical crack growth is expected from H-affected MS-AHSS in the testing conditions analysed by them [56]. These observations suggest that fracture nucleation is the most critical process affected by H. Additionally, Li et al. have argued that plastic damage is required for similar materials to promote H induced-cracking [22,58,59]. The material was characterized by evaluating its standard tensile properties in the SSR regime, and the damage mechanism was identified by fractographic analysis of the fracture surfaces. A material model was applied, which reproduces the specimen's behaviour up to final failure. The material model was then used to predict the results of notched (holed and V-notched) specimens. Data from all three tests was subsequently used to improve the model with the addition of a fracture criterion based upon strain. By analysing the dependence of the model parameters on the H content, strain at fracture was found to be a promising quantity to define a geometry independent HEI. Finally, a test method suitable to accurately estimate the proposed HEI was suggested.

2. Material and methods

2.1. Material

A commercial quenched and tempered MS-AHSS grade 1500 MPa for cold stamping was selected. The material was supplied in zinc-coated rectangular sheets, having dimensions $610 \times 550 \times 1.52$ mm. The microstructure was examined by sectioning the sheets along the rolling and transverse directions. The surfaces were prepared by grinding with SiC waterproof paper ranging from 320 to 1200 grits, and mirror-polishing using a diamond slurry of 1 μm. After chemically etching with Nital reagent (2%), the samples were examined by either optical (Leica DMI3000 M, Leica Microsystems, Wetzlar, Germany) or Scanning Electron Microscopy (SEM), using an FEI Quanta 450 FEG (FEI, Hillsboro, Oregon, USA). Fig. 1(a) illustrates the microstructure observed perpendicularly to the Rolling Direction (RD). As expected, the material presents the typical microstructure of MS-AHSSs, consisting of a martensitic matrix (grey phase) surrounding islands of ferrite (white phase). As shown in Fig. 1(b), the matrix consists of a martensitic lath phase and, since retained austenite was not detected, the austenite was assumed to be fully transformed during quenching. All the observations confirmed that the microstructure was homogeneous with small and rare inclusions.

2.2. Hydrogen charging and measuring

To study the effects of H on the mechanical properties of the alloy, the specimens were electrochemically H charged prior to tensile tests. In order to introduce H into the specimens, zinc-coating was removed using a solution of hydrochloric acid (50% w/w), with hexamethylenetetramine (5 g/L) as a corrosion inhibitor. Residues of the coating were removed by grinding the specimens' surfaces with SiC 500 grits waterproof paper. Finally, the samples were washed in an ultrasonic cleaner. For the electrochemical charging, a solution of 3.5% w/w NaCl was employed [60]. The cathodic current densities j during charging were set to one of two values: 5 mA/cm^2 or 10 mA/cm^2. These relatively low values were chosen in order to keep a low H concentration in the specimen, thus avoiding the risk of producing a severely damaged layer near the surface.

A preliminary estimation, according to the theoretical framework reported in [61] and using data from standard permeation tests not shown in this paper, suggested that a charging time of $T_{ch} = 7$ h is sufficient to obtain a uniform H concentration in the considered media. However, taking into account the trapping effects and the possible differences in the boundary conditions, longer charging times were chosen in order to increase the homogeneity of the concentration and to achieve mean concentrations similar to those commonly produced in components during manufacturing and service [24]. T_{ch} was thus chosen between 16 and 21 h.

To evaluate the effective H concentration in the material at failure, a sample with a mass of approximately 5 g was removed from each specimen near the fracture zone on one of the two halves of the broken specimen immediately after the end of each mechanical test. The other half was used for the fractographic analysis (Section 2.4).

The H concentration was measured using the hot extraction method at a constant temperature [62] using the H analyser LECO DH603 (LECO, St. Joseph, MI). Thermal desorption analysis was performed in order to select the extraction temperature. For this purpose, a sample was cathodically pre-charged in 3.5% w/w NaCl with $j = 10$ mA/cm^2 for $T_{ch} = 21$ h. Fig. 3 shows the H desorption rate as a function of the temperature during heating with a rate of 20 ℃/min. As expected, about 85% of the H was released under 300 ℃. This quantity was considered to be located in reversible trap sites characterized by a low binding energy [63], and thus assumed to have the ability to diffuse in the material at room temperature. The concentration of this part of the total H is called the diffusible H concentration and hereafter is indicated as C_d. The C_d has been correlated with the loss of mechanical properties by several authors [17,20,38,64,65]. The H released at temperatures above 300 ℃ can be considered as strongly trapped at room temperature.

On the basis of this analysis, a hot extraction temperature equal to 265 ℃ was selected in order to measure C_d.

Since the H concentration measurement can usually be performed only after the mechanical test, which was up to one hour, in the worst case, after the end of the H charging process, preliminary tests were
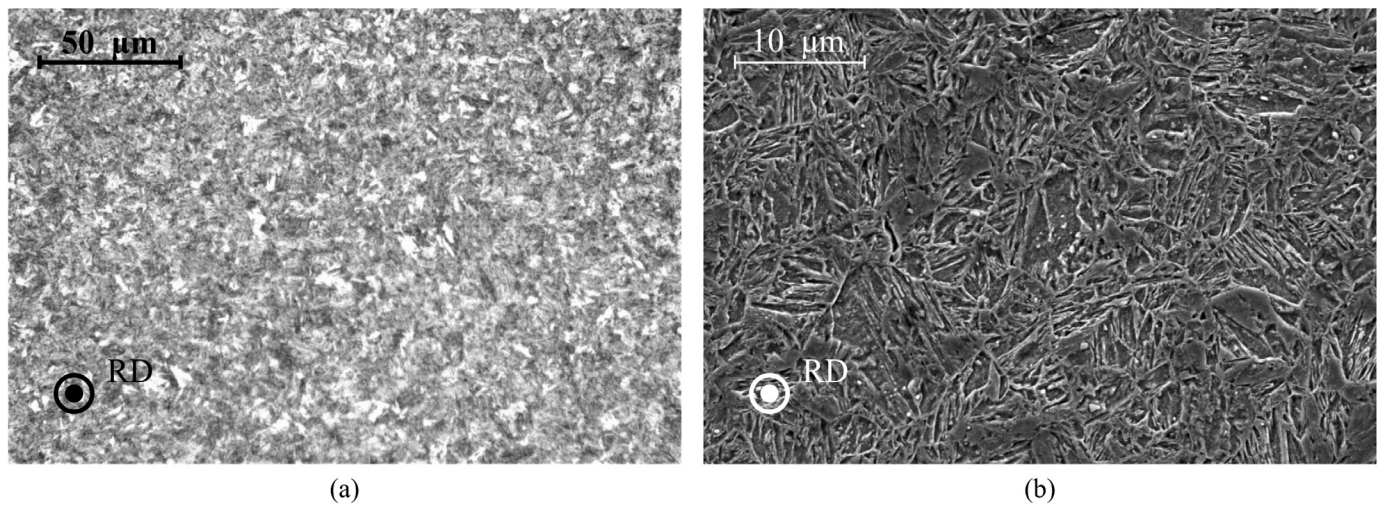
Fig. 1. (a) Optical microscope and (b) SEM micrograph showing the microstructure of the studied alloy along a plane orthogonal to the rolling direction.

conducted to evaluate H loss during this time interval. The H desorption rate in air was thus estimated by measuring the H concentration at different times for two parts from the same specimen after charging. Samples with the geometry and dimensions shown in Fig. 2 were extracted from the sheet, prepared and H charged with the same procedure as the tensile specimens. At the end of the H charging each sample was split into two parts. The H concentration was measured immediately after charging on one part, and after one hour of desorption in air at room temperature on the other one.

Table 1 shows the results of the preliminary H solubility tests, and highlights the effects of the current density j and charging time T_{ch} on C_d. As shown in the table, C_d ranges between 0.4 and 1.3 ppmw. The H lost in the first hour in the air after the end of charging varies from 0.0 to 0.2 ppmw (for the largest initial concentrations), that is an average loss of about 13% of the initial H content. Considering the loss of H, the C_d measured at the end of each mechanical test was assumed to be representative of the average H concentration which was present in the material throughout the test. This simplifying assumption has the consequence that due to H outgassing from the surface, the actual H concentration at fracture was lower than C_d. An accurate evaluation requires a full H diffusion model, taking into account (i) the actual boundary conditions of desorption in air (ii) the H trapping, further complicated by increased dislocation trapping and later microvoid trapping due to plastic strains, and (iii) stress-driven and dislocation-driven H migration [66–71]. Such a model has significant validation problems due to difficulty in measuring local H quantities. With regards to (i), significant discussion and multiple models are present in the literature, some of them highlighting that the boundary conditions are also influenced by hydrostatic stress [53,65,72–83]. Models for boundary conditions in air usually employ Sievert's law which, if H pressure is kept constant, amounts to imposing a constant H concentration on the surface. In our case this would mean imposing zero H concentration on the surface, which would in turn result in a wrong predicted H loss of 46% against the measured 13%.

If we employ the simplified model of evaporation proposed by Crank [61] and calculate the evaporation constant fitting the experimental data, we can obtain a first estimation of the H distribution in the solubility specimen after one hour. The surface H was found to be about 20% lower than the average value. The actual loss in the specimen will be further limited since the test invariably begins within 10 min after the end of H charging, and since due to effect (ii) trapping is increased by plasticity [66,67,69,70].

Table 2 shows the C_d measured after the test for each charged specimen. The electrochemical charging carried out on the specimens produced C_d values comparable to those obtained by the preliminary

Table 1
Results of H solubility tests.

j (mA/cm^2)	T_{ch} (h)	Time in air (h)	C_d (ppmw)		
5	16	0	0.5	0.4	0.7
		1	0.4	0.4	0.6
	21	0	0.7	0.6	0.7
		1	0.6	0.5	0.6
10	19	0	1.1	1.3	0.9
		1	0.9	1.2	0.8
	21	0	1.1	1.3	1.0
		1	1.0	1.1	0.9

Table 2
Post-tensile C_d measured on the samples extracted from the failed specimens.

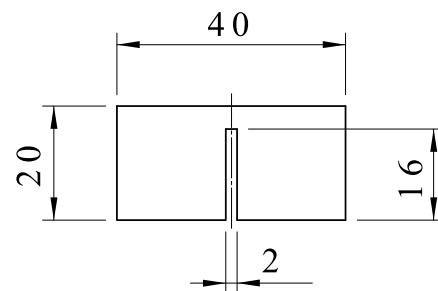| Test type	j (mA/cm^2)	C_d (ppmw)			
UTT	5	0.2	0.5	0.7	0.8
	10	0.9	1.1	1.2	1.5
HTT	5	0.2	0.4	0.5	0.8
	10	0.9	1.1	1.2	1.3
VTT	5	0.1	0.4	0.5	0.7
	10	0.9	1.0	1.1	1.3

Fig. 2. Specimen geometry used for the preliminary solubility testing (dimensions in mm).

solubility tests in the same conditions. Thus, the results of the preliminary solubility tests at zero time in air represent the expected H concentration at the end of the charging process for all specimens.
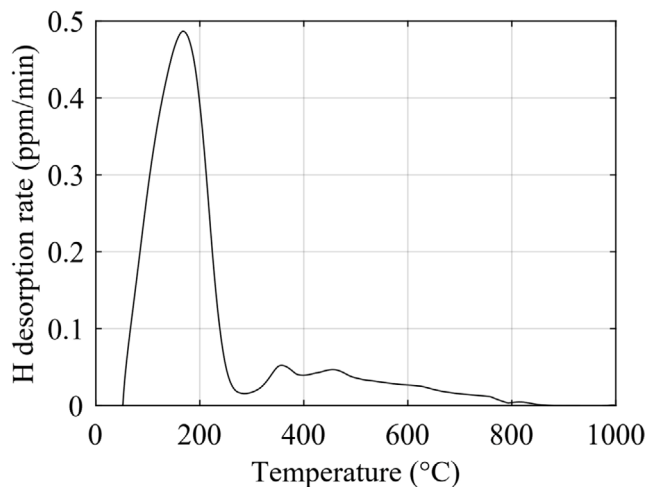
Fig. 3. Thermal desorption analysis results. H desorption rate as a function of the temperature for a heating rate of 20 ℃/min. The sample is cathodically pre-charged in 3.5% w/w NaCl at $j = 10$ mA/cm^2.

2.3. Mechanical testing

Mechanical SSRTs were performed according to ASTM G129-00 [42] on both as-received and H pre-charged specimens. All the specimens were extracted from the metal sheet by laser cutting, with the axis orthogonal to the rolling direction. Zinc-coating was removed before laser cutting using the procedure described in Section 2.2. Tensile SSRTs were performed using a universal servo-hydraulic testing machine MTS 100 kN (MTS Systems Corporation, Eden Prairie, MN) under displacement control with a cross-head speed of 0.001 mm/s. Load and elongation were measured and stored by the Data Acquisition System RT3 (Trio Sistemi e Misure, Dalmine, Italy) at a sample rate of 25 Hz. The tensile properties of the as-received material were identified by analysing the results of three nominally identical tests.

Three geometries were adopted for the specimens (Fig. 4). Each specimen was charged with two values of j (5 mA/cm^2 and 10 mA/cm^2) in order to obtain different nominal C_d values. Each cathodic current/geometry combination was repeated four times. A total of 33 tests were carried out, including those performed on the as-received H free condition.

Un-notched Tensile Tests (UTTs) were performed on specimens shown in Fig. 4(a) in order to assess the effect of C_d on the basic mechanical properties (uniaxial strength and ductility). MTS 634.31F-25 extensometer (gauge length equal to 10 mm) was used to measure the average strain in the reduced section of the specimen during the test. The adopted cross-head speed led to an initial strain rate of 10^{-4} s^{-1}.

Holed Tensile Tests (HTTs) were performed using the specimen as described in SEP1970 [41] and shown in Fig. 4(b). Two pins, inserted in the outermost holes, were used to load the specimen. For this specimen, an extensometer would have measured an averaged strain value in a region with high strain gradients. As a consequence some uncertainty regarding the position of the extensometer arms could have affected the measured displacement, thus amplifying the scatter. The increase in distance between the pins was therefore measured using the Linear Variable Displacement Transducer (LVDT) of the servo-hydraulic testing machine. By processing this signal, repeatable data on the specimen's deformation can be elaborated. More severely notched tensile tests were also considered, using specimens with a couple of V-notches, as shown in Fig. 4(c). These tests are denominated V-notched Tensile Tests (VTTs). The high strain concentration of the specimen was assumed to be characteristic of the most severe notches found in automotive components. MTS 634.12F-24 extensometer (gauge length equal to 25 mm) was used to measure the average strain in the central region of the VTT specimens.

2.4. Fractographic analysis

Fracture surfaces were fractographically analysed by a stereo microscope, after each test and ultrasonic cleaning. A SEM (FEI Quanta 450 FEG) was used to identify the damage mechanism. The fracture surface was captured and the projected area was measured by image analysis using ImageJ software [84]. The fracture initiation and propagation regions were identified.

3. Experimental results

3.1. Un-notched tensile tests

3.1.1. Force-elongation curves

Fig. 5(a) shows the force versus elongation (*F–u*) curve measured for the UTT specimens in the as-received and H charged conditions. The measured C_d (value in ppmw) is reported at the end of each curve. Of the three C_d = 0.0 ppmw curves, only one at is shown in the figure since the difference among them was less than 2%. As expected, H significantly affects the *F–u* curve and the effects depend upon C_d. The most relevant impact is observed on the material ductility, especially on the elongation at fracture. H does not seem to appreciably change the elastic properties and it barely influences the static strain-hardening behaviour at low strains. On the other hand, the post-necking behaviour (present for approximately $C_d \leq 0.9$ ppmw), driven by damage associated with plasticity, is significantly affected. These results are in agreement with common findings in the relevant literature. [21,36,57,65,85].

In Fig. 5(b) the main tensile properties obtained from the analysis of each test are plotted as a function of C_d. In the range analysed, H negligibly reduces YS (from 1371 to 1318 MPa) and UTS (from 1584 to 1508 MPa). On the other hand, the Elongation at fracture (El) and the Reduction in Area (RA) are strongly reduced by the presence of H. In particular, El drops from 9.2% to 1.2%; and RA is reduced until about 1 ppmw (from 36% to 5%). These results highlight that H, in the analysed range of C_d, affects the ductility much more than the strength for this material. Those results suggest that no significant subcritical cracking is present in the UTT specimens. In fact, all curves follow, within reasonable experimental dispersion, the same path up until failure.

3.1.2. Fractographic analysis

Fig. 6 shows the UTT specimens after failure for the as-received condition (a,e) and with different C_d values (b–d,f–h). Fig. 6(a–d) shows lateral profiles of some of the tested specimens. In the as-received condition a cup-cone fracture was observed, which is typical for ductile metallic materials (Fig. 6(a)). A progressive transition from ductile to brittle fracture features can be seen with increasing C_d.

Fig. 6(e–h) shows the frontal view of the fracture surfaces. Solid lines represent the edges of the projected cross-section fractured area, and the dashed lines represent the edges of the undeformed cross-section. The projected fracture surfaces tend to be undeformed as C_d increases. Fig. 7 shows the fracture surface SEM micrograph of the UTT specimens for the as-received conditions and for two H charged conditions in the interval explored. For the specimens with $C_d \leq 0.5$ ppmw, the fracture initiates in the innermost region (identified by the letter A) of the cross-section, where the hydrostatic stress reaches its maximum (Fig. 7(a)), and then propagates through the thickness (identified by the letter B). Both fracture initiation and final fracture regions of the as-received specimen are characterized by the presence of microvoid coalescence dimples (Fig. 7(b,c)).

As shown in Fig. 7(e) for C_d = 0.5 ppmw, fracture nucleates at inclusions producing quasi-cleavage facets. This feature, called fisheye, is located in a portion of the surface with ductile features characterized by microvoid coalescence dimples. Fisheyes, in addition to being nucleation points due to precipitates and H accumulation [86,87],
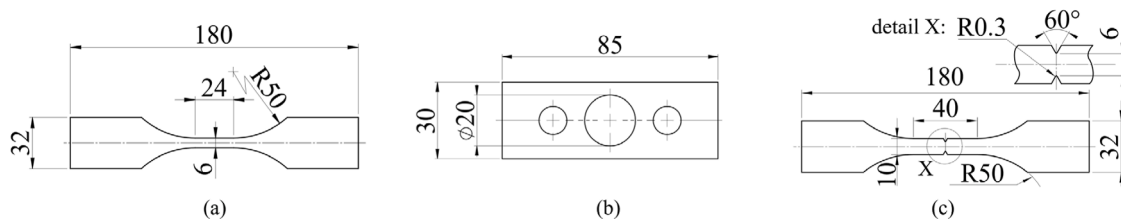
Fig. 4. Specimen geometry and dimensions (in mm) of the specimens (thickness t = 1.52 mm): (a) un-notched, (b) holed and (c) V-notched.
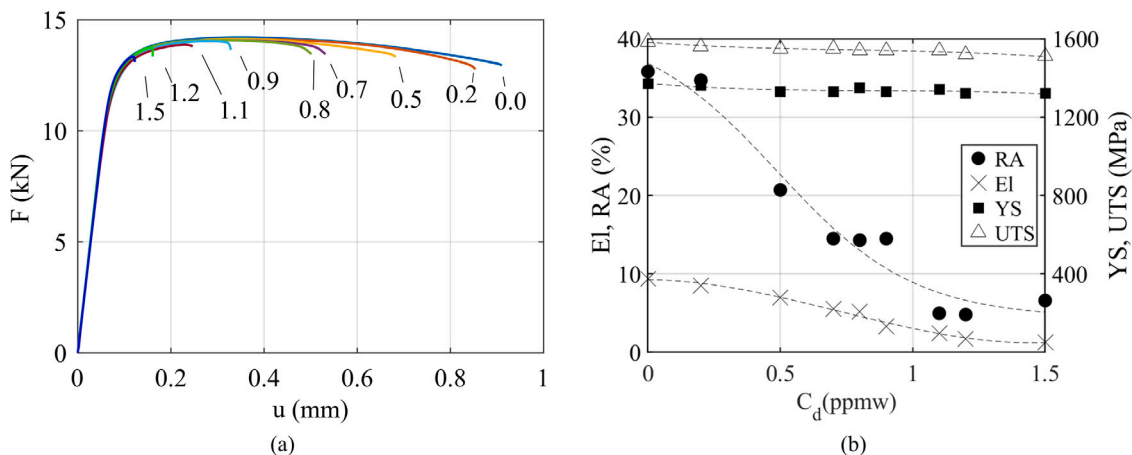

Fig. 5. Experimental results from un-notched tensile tests. (a) Force vs. elongation (*F–u*) curves (the number on each curve indicates the measured C_d in ppmw). (b) Main engineering tensile properties (RA, El, YS and UTS) as a function of C_d.
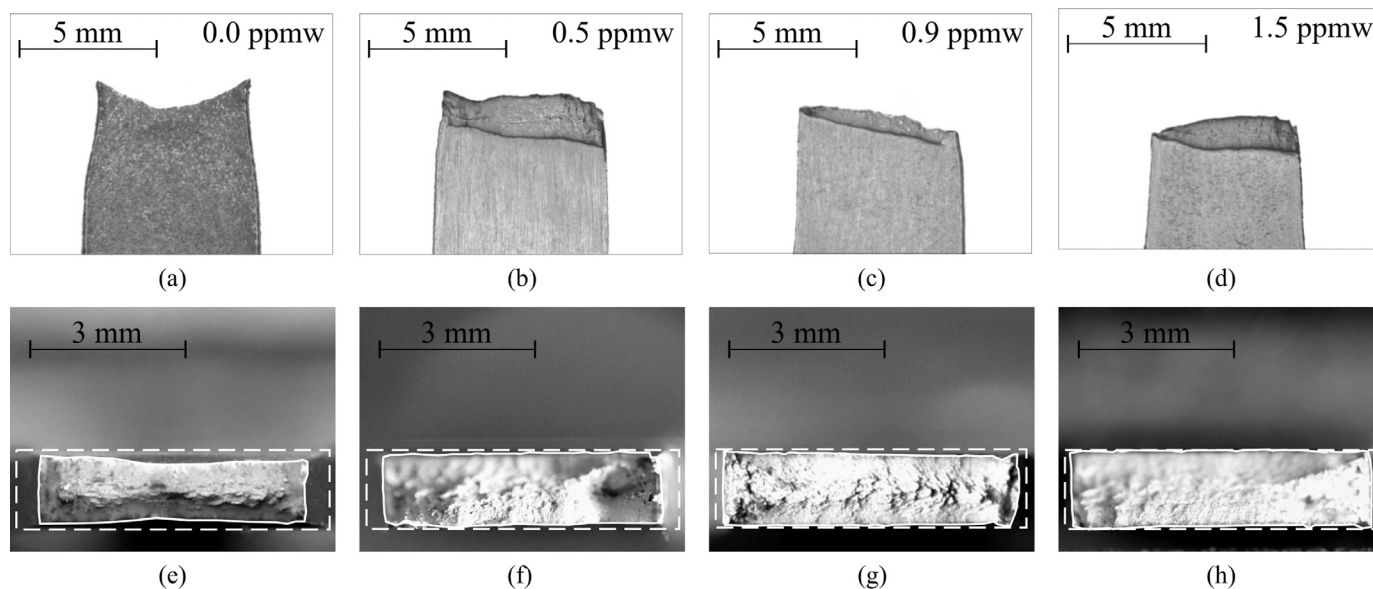

Fig. 6. Fracture surface morphology of Un-notched specimens with 0.0 ppmw (a,e), 0.5 ppmw (b,f), 0.9 ppmw (c,g) and 1.5 ppmw (d,h) of C_d. Lateral views (a,b,c,d) and axial views (e,f,g,h). The solid white lines indicate the edges of the projected cross-sectional fractured area, the dashed lines represent the edges of the undeformed cross-section.

can be formed during final fracture together with the surrounding ductile features [88,89]. The final fracture, far from the initiation point, appears ductile (Fig. 7(f)).

Fig. 7(g) shows the fracture surface for $C_d = 1.5$ ppmw. The fracture initiates on the edge of the cross-section (region *A*) and propagates towards the centre (region *B*). The morphology in the fracture initiation region *A* is characterized by quasi-cleavage with intergranular fracture features (Fig. 7(h)). However, in the rest of the surface

(Fig. 7(i)) the crack propagation is still dominated by microvoid nucleation and coalescence dimples, surrounding uniformly distributed fisheye features.

In conclusion, for the tested material, a transition of the damage mechanism in the crack nucleation region from microvoid coalescence dimples to quasi-cleavage can be observed as C_d increases. The rest of the fracture surface is characterized by mostly microvoid coalescence for all specimens, with the appearance of fisheyes with increasing C_d.
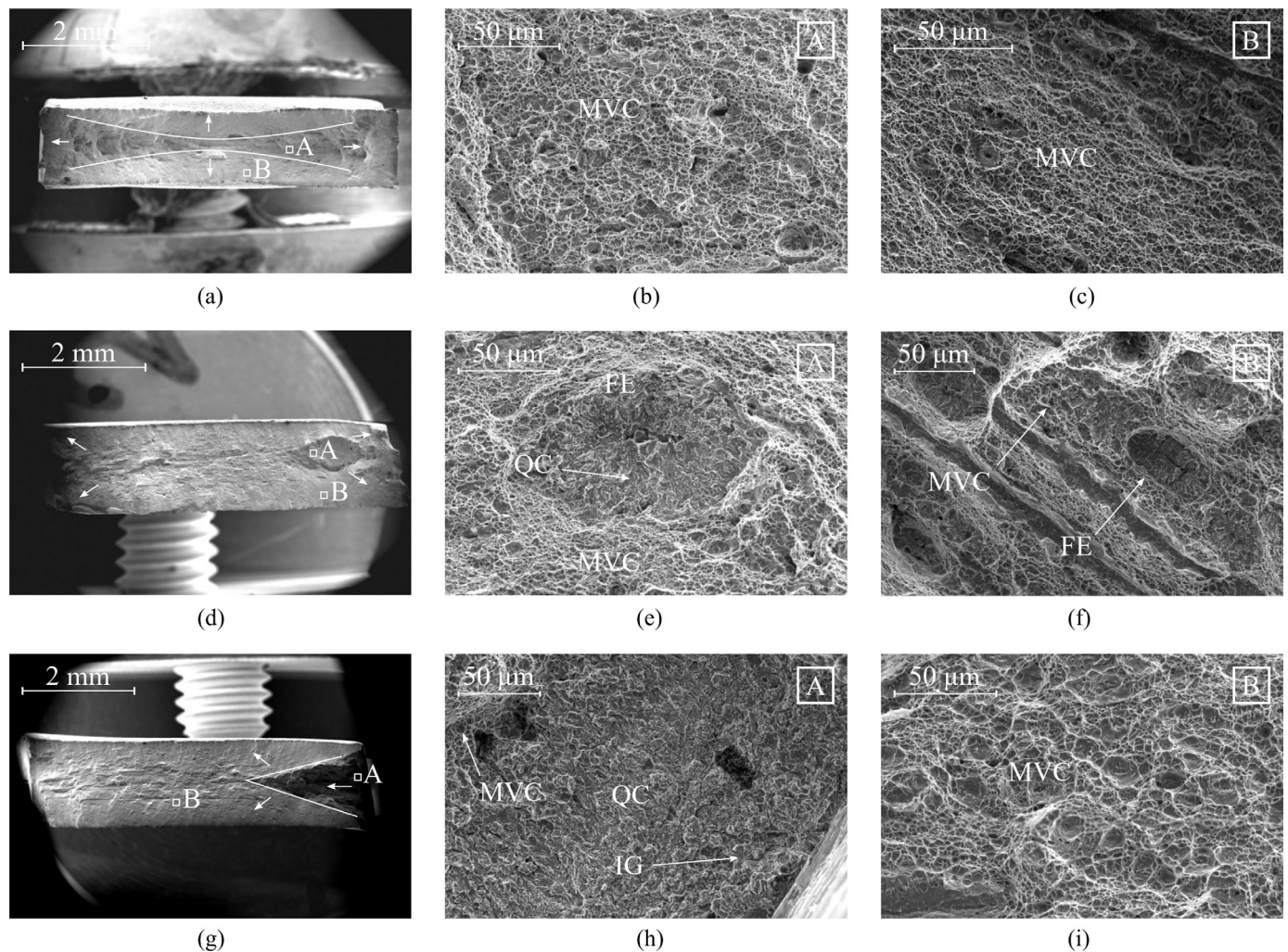
Fig. 7. Fracture surfaces SEM micrographs of the un-notched specimens with $C_d = 0.0$ ppmw (a–c), 0.5 ppmw (d–f), and 1.5 ppmw (g–i). Features such as microvoid coalescence (pointed out by the marker "MVC"), intergranular fracture ("IG"), quasi-cleavage ("QC"), and fisheye ("FE") can be detected.

Since quasi-cleavage features are linked to significant plastic activity [56,57,90,91], in spite of the appearance of intergranular features, the fracture mechanism is governed by plasticity for each C_d analysed, thus indicating that H likely interacts with dislocation mobility, similarly to the HELP mechanism [21,24]. The average size of the microvoid coalescence dimples tends to increase with increasing C_d (Fig. 7(c,f,i)). This also indicates the uniform influence of H on the entire cross-section. In addition, the migration of the fracture initiation region from the centre to the sides of the specimen suggests that surface effects (e.g. roughness, edges) become more relevant with increasing C_d. A similar behaviour was observed by Venezuela et al. in MS-AHSS [56,57]. Kan et al. [71] have shown that H transport towards the centre of the specimen due to hydrostatic stress gradient can significantly influence the test results. In their case, they found extensive brittle fracture at the centre due to slower strain rates and higher H concentration, but in principle the results agree that fracture initiation from the centre can be expected for some hydrogen-charged un-notched tensile tests.

3.2. Notched tensile tests

3.2.1. Holed tensile tests

Three HTTs were performed on the as-received material in order to obtain the reference *F–u* curve. Fig. 8 reports the experimental force versus displacement (*F–u*) curves from H charged HTT. The test

rig compliance was neglected. A standard deviation of 0.4 kN on the maximum measured force (1.7% of the mean) was determined.

After an initial linear response, a non-linear trend of the *F–u* curve with decreasing slope can be observed up to a maximum, where necking starts. A post-necking descending trend leading to specimen failure is observed. Similarly to the un-notched specimens, the presence of H reduces the displacement at fracture. In fact, as C_d increases up to 0.5 ppmw, the last region of the curve characterized by necking progressively tends to disappear and the maximum and fracture points tend to overlap. For $C_d \geq 0.9$ ppmw the transition to brittle macroscopic behaviour is completed, and fracture occurs in the linear regime. As shown in Fig. 8(b), the most significant effect of C_d is the drop in material ductility. It can be concluded that H affects the HTT in the same way as with the UTT.

The analysis of the fracture surfaces of the HTT specimens confirms this similarity (Fig. 9). The main difference is the position of the fracture nucleation site (region *A*), which, due to the geometry, is located at the notch root for any H concentration. Fig. 9 (a–c) shows the fractography of the HTT with $C_d = 0.0$ ppmw. Fracture initiation was at the notch root and the fracture surface was characterized by ductile dimples. Fig. 9 (d–f) shows the fractography of the HTT with $C_d = 1.3$ ppmw. Fracture initiation at the notch root was characterized by a transition from intergranular, quasi-cleavage to ductile dimples. The rest of the fracture surface showed ductile dimples with some fisheyes and secondary cracks along the rolling direction probably due
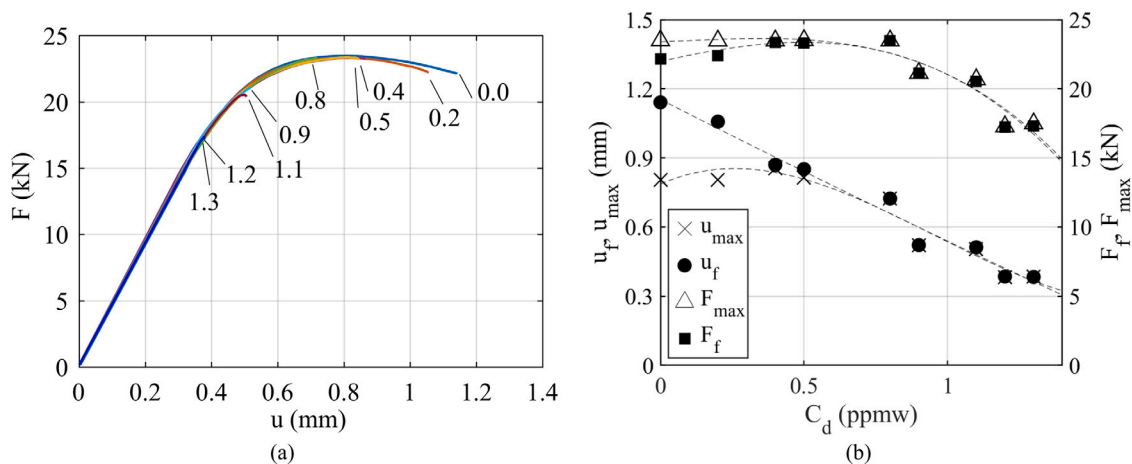
Fig. 8. Holed tensile test results. (a) Experimental force vs. elongation *F–u* curves (the number on each curve indicates the measured C_d value in ppmw). (b) Force and displacement values at maximum force (u_{max}, F_{max}) and fracture conditions (u_f, F_f) as functions of C_d.
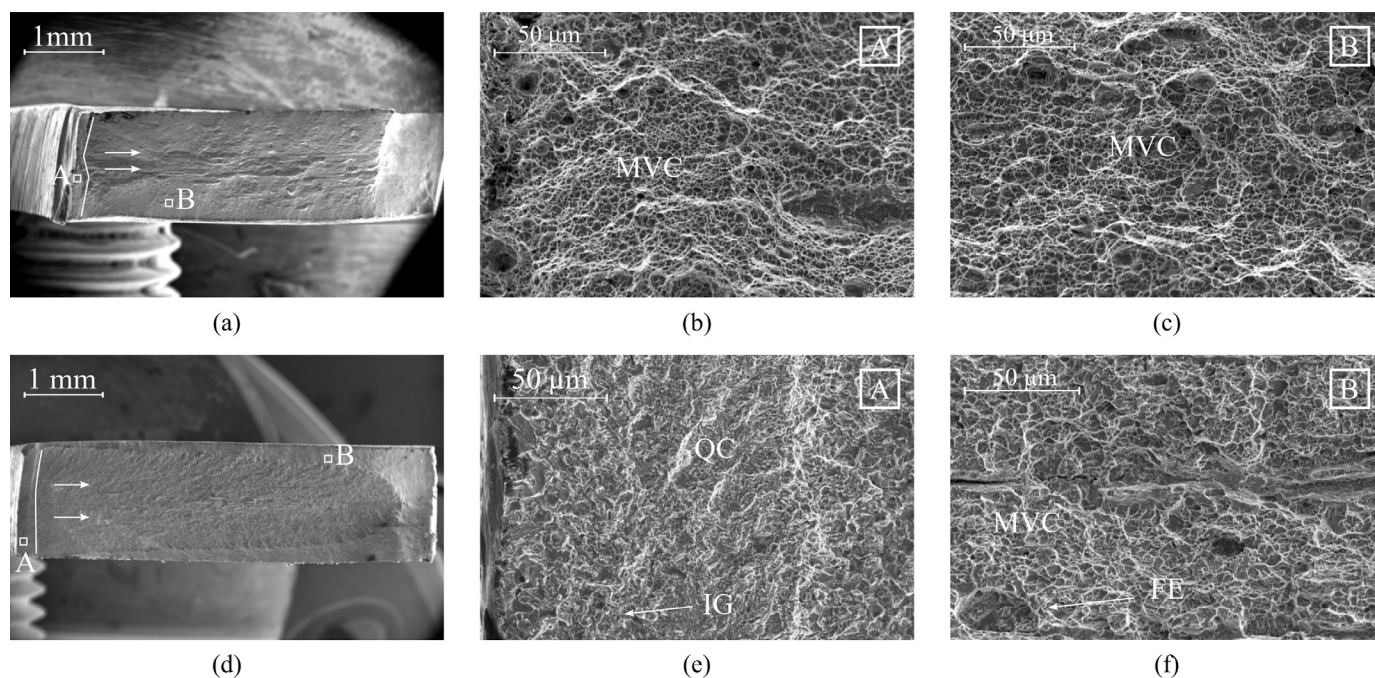

Fig. 9. Fracture surface SEM micrographs of the holed tensile test specimens with 0.0 ppmw (a–c) and 1.3 ppmw (d–f). Region *A* refers to the crack nucleation site, region *B* to the crack propagation. Features such as microvoid coalescence (pointed out by the marker "MVC"), intergranular fracture ("IG"), quasi-cleavage ("QC"), and fisheye ("FE") can be detected.

to aligned precipitates. The intermediate specimens showed the same trend that was found for UTT: a progressive appearance of brittle features. It can be concluded that the influence of H does not seem to be significantly changed in presence of notches with moderate stress concentration.

3.2.2. V-Notched tensile tests

Fig. 10(a) shows the force versus elongation (*F–u*) curves obtained from the VTT specimens for the as-received material and different C_d values. The effect of H on the tensile curves is similar to that obtained with HTT specimens (Fig. 8). Again, there are three distinct regions in the *F–u* curves: a linear response, a non-linear behaviour characterized by a decreasing slope up to a maximum, and a descending part up to the final fracture. As the last part of the curve has a weak decreasing trend, the force at failure is only slightly smaller than the maximum value. As C_d increases, the second and third regimes tend to disappear.

For $C_d > 0.7$ ppmw, the fracture occurred at the maximum force, thus indicating the absence of the third regime. In Fig. 10(b) the force and displacement values corresponding to the maximum and fracture conditions are plotted versus C_d.

Fig. 11 shows the fracture surface SEM micrograph of the VTT specimens in as-received conditions (a–c) and for $C_d = 1.3$ ppmw (d–f). On the left: a macroscopic view of the fracture surface. For both conditions, the fracture initiates at the notch tip (Fig. 11(a,d)). The fracture surface features are similar to those observed in un-notched tensile specimens. In the as-received conditions, the whole observed fracture surface is characterized by the presence of microvoid coalescence dimples (Fig. 11(b,c)). For the $C_d = 1.3$ ppmw, the fracture initiation region has brittle features characterized by the presence of quasi-cleavage (Fig. 11(e)). The final fracture shows fisheyes surrounded by microvoid coalescence dimples.
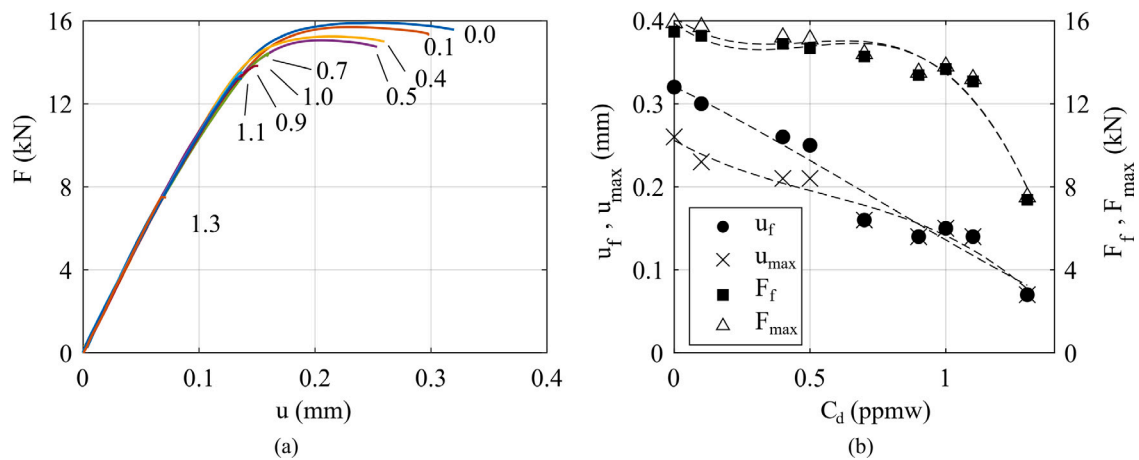
Fig. 10. V-Notched tensile test results. (a) Experimental force vs. elongation (*F–u*) curves (the number on each curve indicates the measured diffusible H concentration C_d in ppmw). (b) Force and displacement values at maximum force (u_{max}, F_{max}) and fracture conditions (u_f, F_f) as functions of C_d.
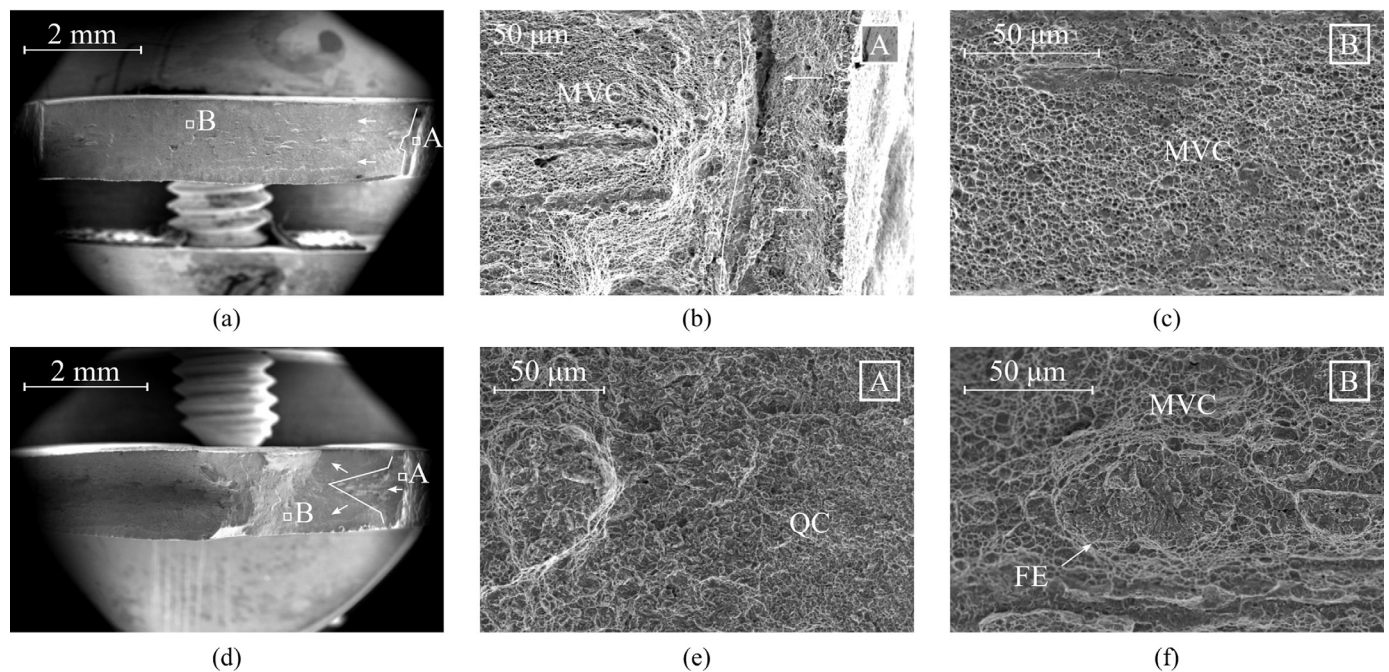

Fig. 11. Fracture surface SEM micrographs of the V-notched tensile test specimens with 0.0 ppmw of diffusible H concentration (a–c) and 1.3 ppmw (d–f). A macroscopic view of the fracture surface it is presented on the left, where the arrows indicate the fracture propagation direction. The fracture initiation region is shown in the centre, and on the right the fracture region far from it. Features such as microvoid coalescence (pointed out by the marker "MVC"), quasi-cleavage ("QC"), and fisheye ("FE") can be detected.

4. Discussion

The results obtained from UTTs (Fig. 5 (a,b)) reveal that, in tensile tests, H mostly influences the necking and post-necking response, since the *F–u* curves follow the same path for every C_d at least up until necking is reached. A progressive transition from ductile to brittle macroscopic behaviour was observed. Fractographic analysis shows that away from the fracture nucleation area, the damage process and final fracture are driven by plasticity for each specimen and for each C_d, since there are always microvoid dimples and quasi-cleavage features. The final fracture nucleation sites exhibit prominent brittle quasi-cleavage or intergranular features as C_d increases, the former of which is still linked to significant localized plastic flow [56,57,90,91]. Similar remarks apply to the results for HTT and VTT. Only the HTT and VTT specimens with $C_d \geq 1.3$ ppmw show fracture nucleation sites dominated by quasi-cleavage, with no significant plastic damage.

In order to identify a suitable test-independent material property to be used for the evaluation of the HEI, an H-dependent material model was developed that captures the whole mechanical response observed in the performed tests up to failure. The material model includes the following components:

- true $\sigma - \varepsilon$ elastoplastic law
- damage model
- fracture criterion

The first two components in the model were first calibrated using the UTT test data, since this test provides the most direct information.

The model was then used to predict the experimental data in HTT and VTT tests, and it was validated by comparing experimental and predicted results up to, but not including, specimen failure.

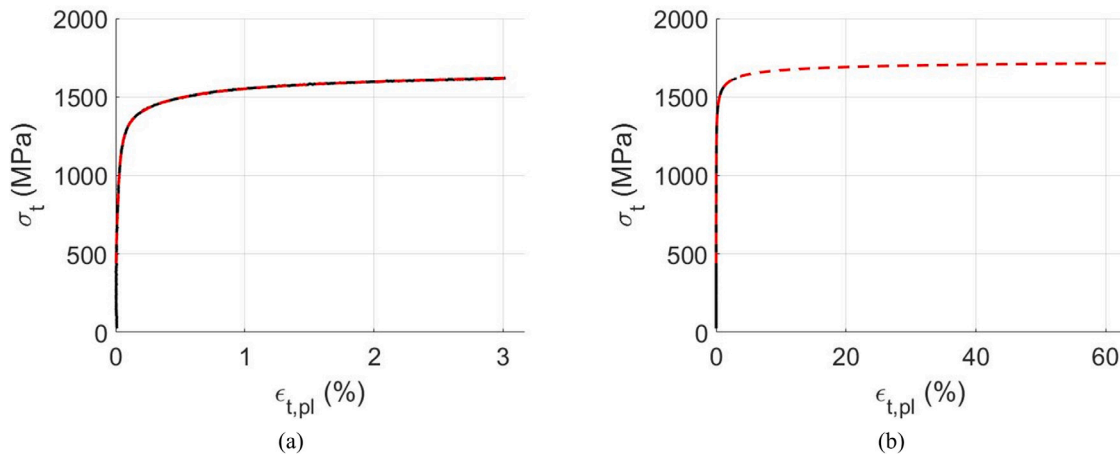With regards to the definition of the fracture criterion, experimental data from all tests were subsequently used.

Fig. 12. Approximation of the experimental true stress - true plastic strain data, black solid line, with the model in Eq. (1), red dashed line, (a); extrapolation of the constitutive curve up to a strain value of 60% (b).

4.1. Elastoplastic stress–strain relationship

The basic elastic behaviour of the material and its strain hardening law have to be identified. Some researchers have found that elastic parameters [92] or yield stress [93,94] may be influenced by H. For the tested material no such effect appears to have been measured, as confirmed by other researchers [22,55–57]. Consequently it would seem that the elastoplastic behaviour is not significantly influenced by H.

Up to the maximum force point of the averaged UTT F–u curve for $C_d = 0.0$ ppmw the true stress-true plastic strain (σ_t, $\varepsilon_{t,pl}$) curve was calculated as:

$$\sigma_t = \frac{F}{A_0}(1 + \frac{u}{u_0})$$

and

$$\varepsilon_{t,pl} = \ln(1 + \frac{u}{u_0}) - \frac{\sigma_t}{E}$$

where u_0 is the initial gauge length, A_0 the initial cross-section area and E Young's modulus.

The experimental data were fitted by employing various analytical expressions proposed in the literature. The best results were obtained with the following combination of Swift's and Voce's hardening laws, which has been widely used for modelling the hardening behaviour of sheet metals [95–97]:

$$\sigma_t = \sigma_0 + K_1(\varepsilon_0 + \varepsilon_{t,pl})^n + K_2[1 - \exp(-\lambda \varepsilon_{t,pl})] \tag{1}$$

with:

$\sigma_0 = 1020$ MPa, $K_1 = -40.6$ MPa, $K_2 = 742.3$ MPa,

$\varepsilon_0 = 3.7 \cdot 10^{-4}, n = -0.36, \lambda = -4864$

The Swift component is needed in order to represent the hardening part at the end of the curve, since the Voce term rapidly converges to a constant value. The Voce term models the rapid increase in flow stress for very small plastic strains. The proposed approximation is able to represent the mechanical behaviour of the tested material, at least up to the necking point, with less than 0.5% error. The high level of accuracy further suggests that Eq. (1) can be tentatively extrapolated to investigate the material response at large plastic strains, approaching the fracture nucleation. Fig. 12 demonstrates the agreement between experimental and calculated $\sigma_t - \varepsilon_{t,pl}$ curve (a), and the extrapolated constitutive curve up to 60% (b). As expected, the UTT with $C_d = 0.0$ ppmw can be correctly reproduced by using exclusively Eq. (1), with the exception of the last 0.3 mm of the curve, where the specimen has a slightly lower strength than predicted. This stress reduction can be explained by a spread of damage due to the high level of plastic strain.

4.2. Gurson's model

The experimental evidence suggests that plastic damage can be modelled by adopting Gurson's model as modified by Tvergaard and Needleman (GTN model) [98,99]. Gurson's and the GTN models have already been employed by various researchers for the modelling of HE [100–104]. According to the model, the yield locus Φ is influenced by the void volume fraction f as follows:

$$\Phi(\sigma_{ij}, \sigma_y, f) = \left(\frac{\sigma_{eq}}{\sigma_y}\right)^2 + 2fq_1 \cosh\left(\frac{3q_2\sigma_h}{2\sigma_y}\right) - (1 + q_3f^2) \tag{2}$$

where σ_{eq} is the Von Mises equivalent stress, σ_h is the hydrostatic stress, σ_y is the material flow stress in the absence of voids, and q_1, q_2 and q_3 are material constants [105]. The increasing time rate $\dot{f}$ of the void volume fraction is obtained by the sum of two contributions: the growth rate of voids $\dot{f}_g$ and the nucleation rate of new voids $\dot{f}_n$, given by:

$$\dot{f}_g = (1 - f)\dot{\varepsilon}_{kk}^p \tag{3}$$

$$\dot{f}_n = \frac{f_N\dot{\bar{\varepsilon}}^p}{S_N\sqrt{2\pi}}\exp\left(-\frac{1}{2}\left(\frac{\bar{\varepsilon}^p - \varepsilon_N}{S_N}\right)^2\right) \tag{4}$$

where $\dot{\bar{\varepsilon}}^p$ is the time rate of the equivalent plastic strain $\bar{\varepsilon}^p$, f_N is the volume fraction of void nucleating particles, ε_N and S_N are the mean strain and the standard deviation of the nucleation rate of voids, and $\dot{\varepsilon}_{kk}^p$ is the trace of the plastic strain rate tensor. The GTN model is completely defined when the parameters f_0, q_1, q_2, q_3, ε_N, f_N, S_N are given. Since damage initiation and evolution are influenced by C_d, in principle all the parameters in the GTN model may depend on it.

Since the manufacturing process does not generate initial porosity, it is reasonable to assume that $f_0 = 0$.

The parameters q_1, q_2 and q_3, as indicated by Tvergaard [105], are dimensionless constants equal to 1.5, 1.0 and 2.25, respectively. As a consequence ε_N, f_N and S_N are the model parameters to be determined for each C_d. For the sake of simplicity we assume that C_d is homogeneous and constant throughout the test and in the whole domain. This assumption, which is not unreasonable considering the level of the expected outgassing (see subsection Section 4.4) allows to model the process by using the available commercial software.

In order to identify these parameters, an optimization algorithm was adopted that minimizes the mean square root difference between experimental and predicted F–u curves. A three-dimensional Finite Element Model (FEM) was set up, implemented in *Ansys® Academic Research Mechanical, release 19.1*, in a domain reproducing the specimen geometry as shown in Fig. 13(a). The model employed 8-nodes structural solid elements having three degrees of freedom at each node. Symmetries were
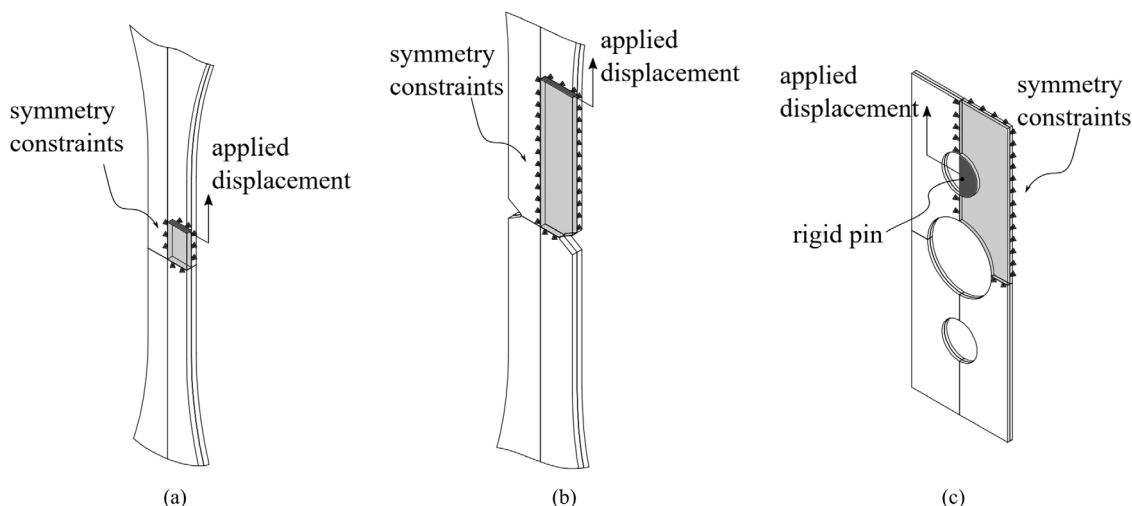
Fig. 13. Finite element model geometries of the un-notched (a), V-notched (b) and holed specimen (c).
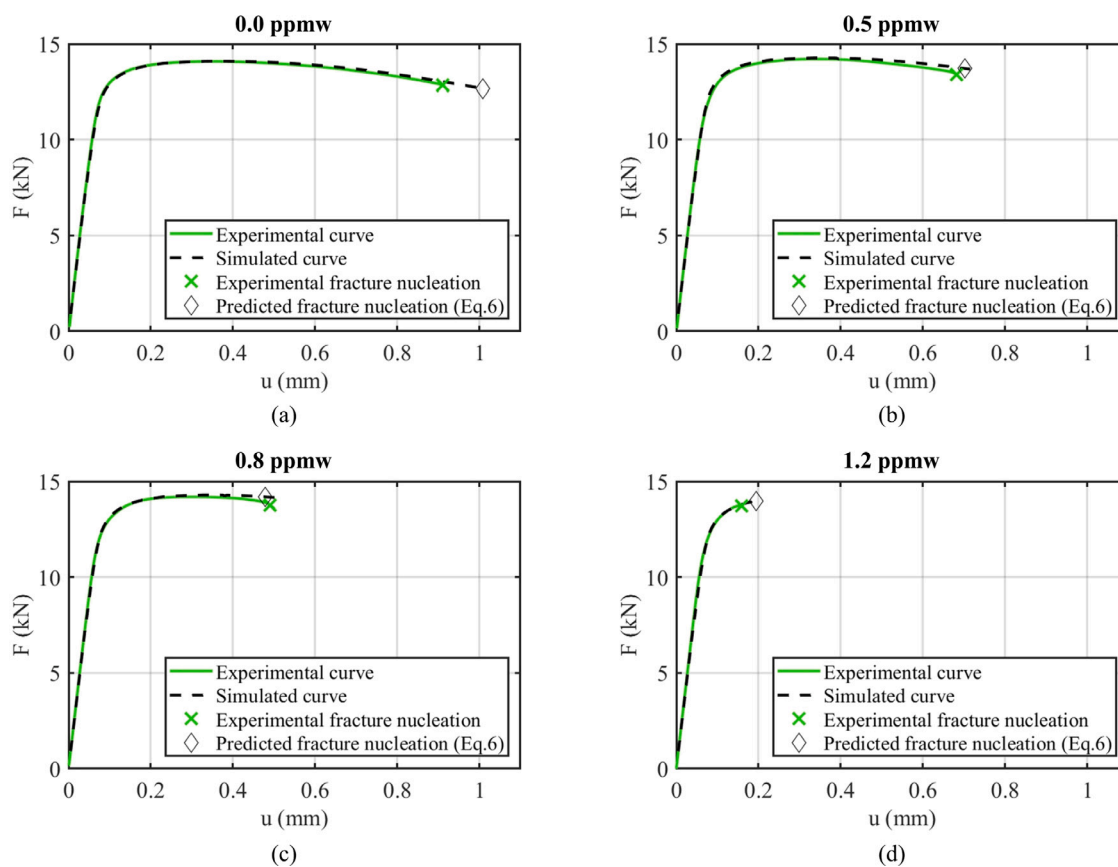

Fig. 14. Comparison between experimental and simulated un-notched tensile test force vs. elongation (*F–u*) curves for measured C_d values varying from 0.0 to 1.2 ppmw. As described in Section 4.4, experimental and simulated nucleation points refer to the process of estimating the fracture nucleation strain ε_f from the curves, while diamonds are the fracture nucleation points predicted by the fitted $\varepsilon_f = f(C_d)$ law (Eq. (6)).

exploited to minimize the computational cost of the model, as shown in Fig. 13. To account for manufacturing variability, the geometry of each specimen was measured before the test and reproduced in the FEM model. Since no fracture criterion was introduced, the numerical simulation was allowed to progress beyond the experimentally observed failure condition. Fig. 14 compares the experimental and simulated *F–u* curves of the UTTs for some C_d, using the identified model parameters. The good agreement confirms the validity of the proposed model and of the identification procedure adopted.

The mean nucleation strain ε_N was found to be reasonably reproduced by a linear function of C_d in the examined range (Fig. 15(a)):

$$\varepsilon_N(\%) = -10.6 \cdot C_d + 14.1 \qquad C_d \leq 0.8 \tag{5}$$

The identified parameters f_N and S_N were equal to 0.012 and 0.05, respectively. The damage associated with microvoid nucleation and growth does not significantly affect the *F–u* curve when $C_d > 0.8$ ppmw. For this reason, only the points in the interval between 0.0 and 0.8 ppmw of C_d were considered.
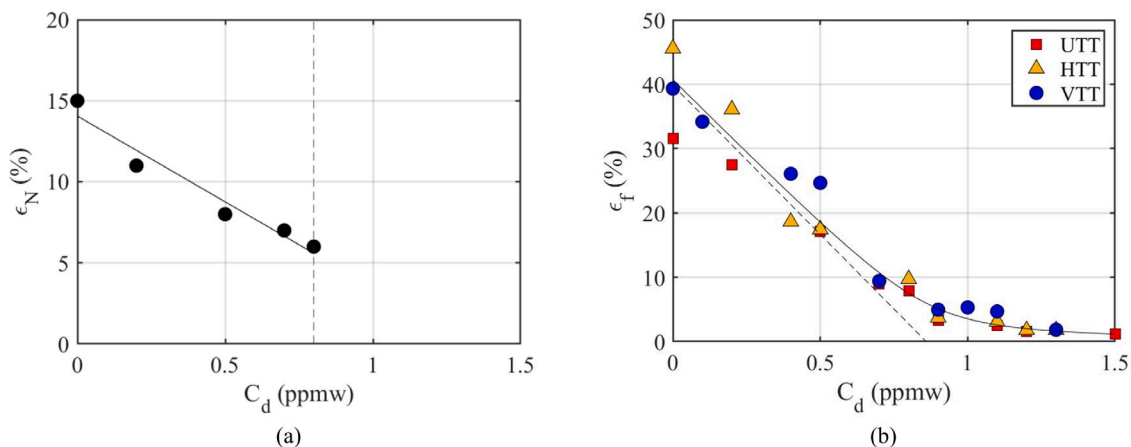
Fig. 15. Constitutive model parameters as a function of the average diffusible H concentration (C_d). (a) Void nucleation strain (ε_N) calculated reproducing un-notched tensile tests and linear fit from Eq. (5). (b) First principal strain at fracture (ε_f) from simulated fracture nucleation points and fit from Eq. (6).

4.3. Notched tensile tests simulation

The constitutive model was subsequently used to simulate VTTs and HTTs. The geometries (Fig. 13(b,c)) of the two specimens were reproduced by a FEM similar to the one used for the UTTs. For HTTs, a correction term for the test rig compliance was necessary, since the model assumed rigid pins and did not include any other part of the test rig. For this purpose, the test rig was assumed to be a linear spring in series with the specimen. The equivalent spring constant k was estimated by comparing the experimental data and the numerical predictions in the linear regime. A compliance correction equal to kF was added to the simulated displacement on each HTT curve. Fig. 16 and Fig. 17 compare the experimental and simulated F–u curves from HTTs and VTTs, respectively. The model shows a good agreement with experimental results for the notched specimens. The ability to quantitatively reproduce the experimental results for all the three types of notched specimens suggests that none (including the most severe) had experienced significant sub-critical crack growth. Indeed, sub-critical crack growth has been mostly detected when performing in-situ charging and with slower strain rates [26,45,52,106] than our 10^{-4} s^{-1}, while in the present work the specimens were electrochemically pre-charged and then mechanically tested in air. Furthermore, in the investigated case the occurrence of an extensive sub-critical crack growth would imply that the crack front would need to stop while propagating from the specimen surface, subjected to the outgassing effect, towards brittle areas with higher H concentration.

4.4. Fracture criterion

As no significant subcritical crack growth was observed nor expected in the tested conditions, the focus was on the conditions for crack nucleation. In order to introduce fracture nucleation into the model, a fracture criterion was needed. In the literature various approaches have been used to model fracture [107] For the tested material, the experimental results show that C_d does not significantly affect tensile strength, whereas ductility properties are affected. A strain-based fracture criterion therefore seems a simple yet appropriate approach, and it has already been implemented to study HE [94,108–110]. Since stress is predominantly uniaxial where the fracture initiation occurs, the associated strain component, namely the maximum principal strain (ε_1), is the simplest promising quantity to be used as a fracture predictor. Hence, according to the implemented criterion, the fracture initiation critical condition is reached when $\varepsilon_1 = \varepsilon_f$, where ε_f is a material property representing strain at fracture nucleation, whose value depends on C_d. Crack initiation is quickly followed by final fracture.

In order to estimate ε_f, each experimental curve was inspected for signs of failure, such as a significant downward slope change or, possibly, sudden force drop. This location on each F–u curve was marked as the "experimental fracture nucleation" point. The nearest simulated point on the F–u curve was subsequently identified and its corresponding maximum nodal ε_1 value was exported from the FEM as an estimation of ε_f.

Fig. 15(b) shows the dependence of ε_f upon C_d. Two regimes can be identified. For $C_d \leq 0.9$ ppmw, strain at fracture steeply decreases (from 42% to about 5%) following a linear trend, while for $C_d > 0.9$ ppmw the slope of the fitting curve significantly reduces. To reproduce this dependence, a hyperbola was fitted with one horizontal asymptote at $\varepsilon_f = 0$:

$$C_d = 0.8778(1 - \frac{\varepsilon_f}{\varepsilon_{f0}}) + \frac{1}{53.119}(\frac{\varepsilon_{f0}}{\varepsilon_f} - 1) \tag{6}$$

where $\varepsilon_{f0} = 40.7\%$ is ε_f at $C_d = 0.0$ ppmw. It is worth remarking that C_d is the H concentration measured by hot extraction method and not the local H concentration at the fracture nucleation site. In Figs. 14, 16 and 17, a hollow diamond marks the location on the simulated F–u curves where fracture nucleation is predicted by using Eq. (6), or the "Predicted fracture nucleation" point.

Fig. 18 shows the correlation between predicted and experimental F and u values at fracture nucleation for each curve.

Fig. 19 shows the contour plots of ε_1 for UTTs at fracture initiation for three values of C_d.

Fig. 19(a, b) compares the conditions at fracture initiation in the specimen in the as-received conditions and with $C_d = 0.5$ ppmw. The ε_1 is at its maximum in the centre of the specimen. This phenomenon occurs for specimens showing necking (up to 0.8 ppmw). In specimens with a higher C_d (from 0.8 to 1.3 ppmw), as can be seen in Fig. 19(c), the ε_1 is uniform throughout the gauge length of the specimen with a slight strain concentration on the external surface. In the tested conditions, the point of maximum first principal strain coincides with the fracture initiation point observed by fractographic analysis. It is worth mentioning that if H was continuously created on the surface during the test, the surface would probably represent the fracture initiation point for each H-charged specimen.

Fig. 20 shows the void volume fraction f at fracture initiation for the specimen in as-received condition (a–c) and with $C_d = 0.5$ ppmw (d–f). With the same C_d, the void volume fraction value at fracture is similar for all types of tests. However, as the notch severity increases, the volume of material subject to high void volume fraction decreases, until it can be safely assumed that porosity, and therefore the GTN damage model, has no significant impact on the macroscopic F–u curve.
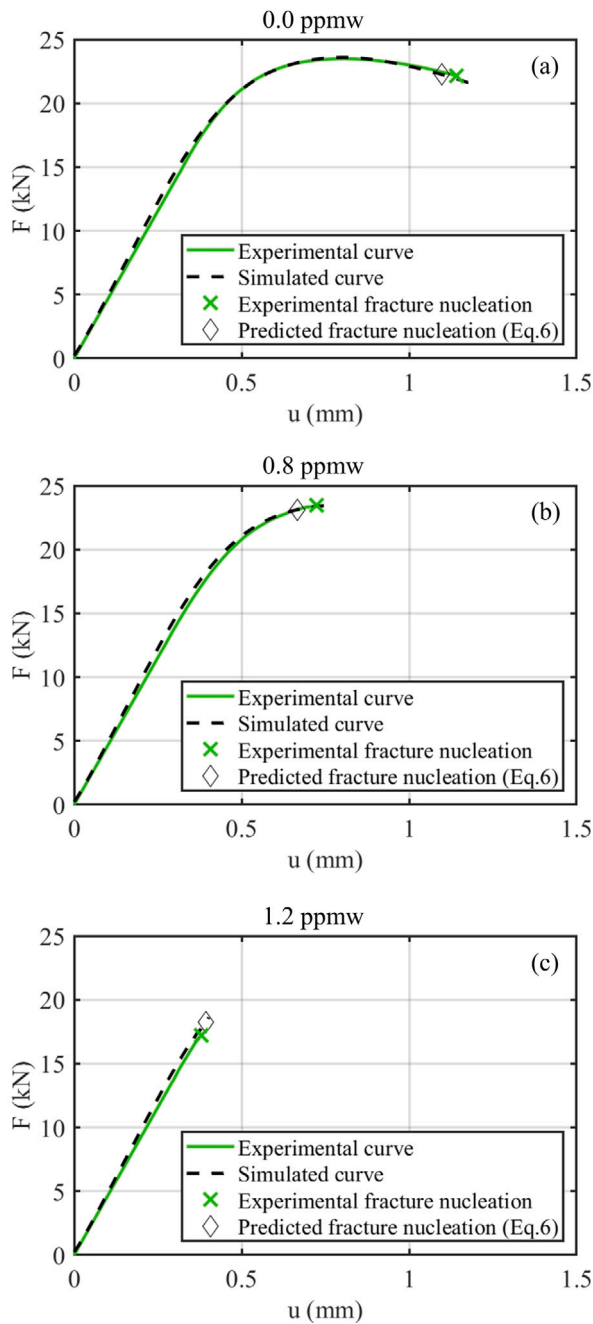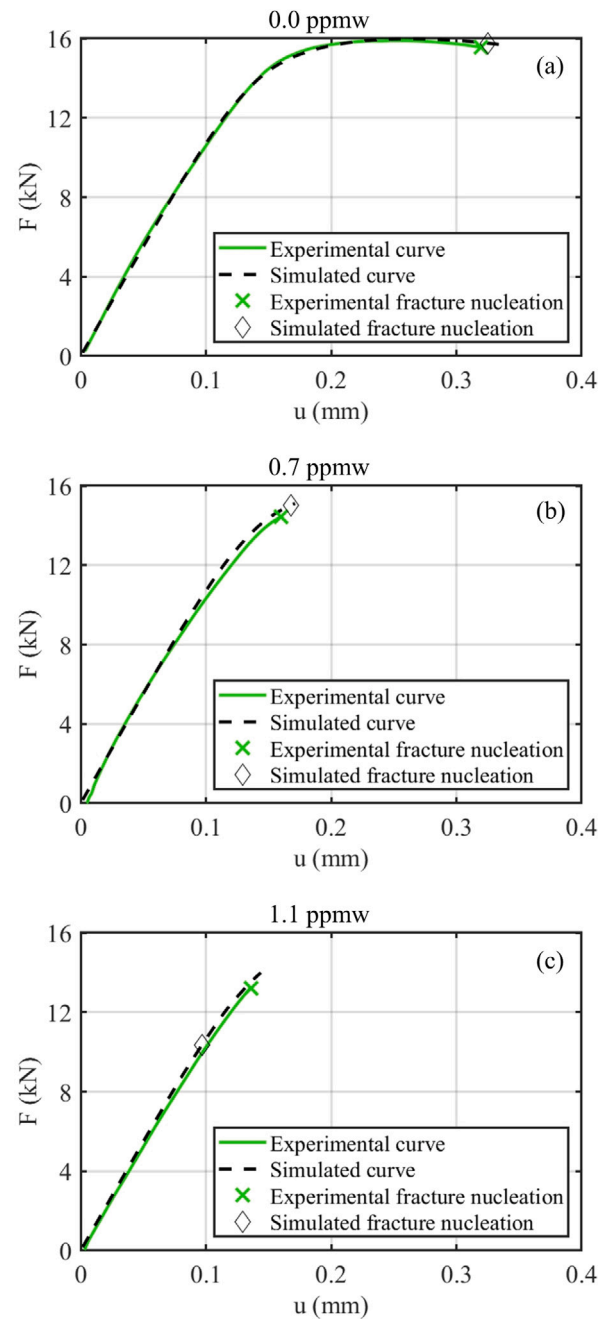
Fig. 16. Comparison between three experimental and simulated holed tensile test force vs. elongation *F–u* curves for a few measured diffusible H concentration (C_d) values in ppmw. As described in Section 4.4, experimental and simulated nucleation points refer to the process of estimating the fracture nucleation strain ε_f from the curves, diamonds are the fracture nucleation points predicted by the fitted $\varepsilon_f = f(C_d)$ law (Eq. (6)).

Fig. 17. Comparison between three experimental and simulated V-notched tensile test force vs. elongation (*F–u*) curves for a few measured diffusible H concentration (C_d) values in ppmw. As described in Section 4.4, experimental and simulated nucleation points refer to the process of estimating the fracture nucleation strain ε_f from the curves, diamonds are the fracture nucleation points predicted by the fitted $\varepsilon_f = f(C_d)$ law (Eq. (6)).

5. Hydrogen embrittlement index

The HEI measures the reduction of a chosen material property linked to failure (ϕ_f) in an H-charged specimen $\phi_{f,H}$, relatively to the same property in the H-free case $\phi_{f,F}$ by the following formula:

$$\text{HEI} = \frac{\phi_{f,F} - \phi_{f,H}}{\phi_{f,F}} \tag{7}$$

Various tests and material properties have been used to quantify the degradation of the material mechanical properties due to H. The reduction in area *RA* observed in standard tensile tests is often chosen

for ϕ_f [16]. Among other possible choices for ϕ_f are maximum stress, fracture toughness, elongation at fracture, uniform elongation. As *RA* is a technological property, it manifestly depends upon the adoption of a standardized specimen and test rig. Therefore, in principle, it cannot be compared with results obtained from holed or notched specimens. The definition of the HEI can be improved by basing it upon a suitable constitutive parameter, which behaves consistently over different tests. Two mechanical properties have a significant dependence on C_d: the mean void nucleation strain ε_N and the maximum principal strain at fracture ε_f. However, ε_N, is a parameter that controls elastoplastic damage, and is only able to model the most ductile material behaviour.
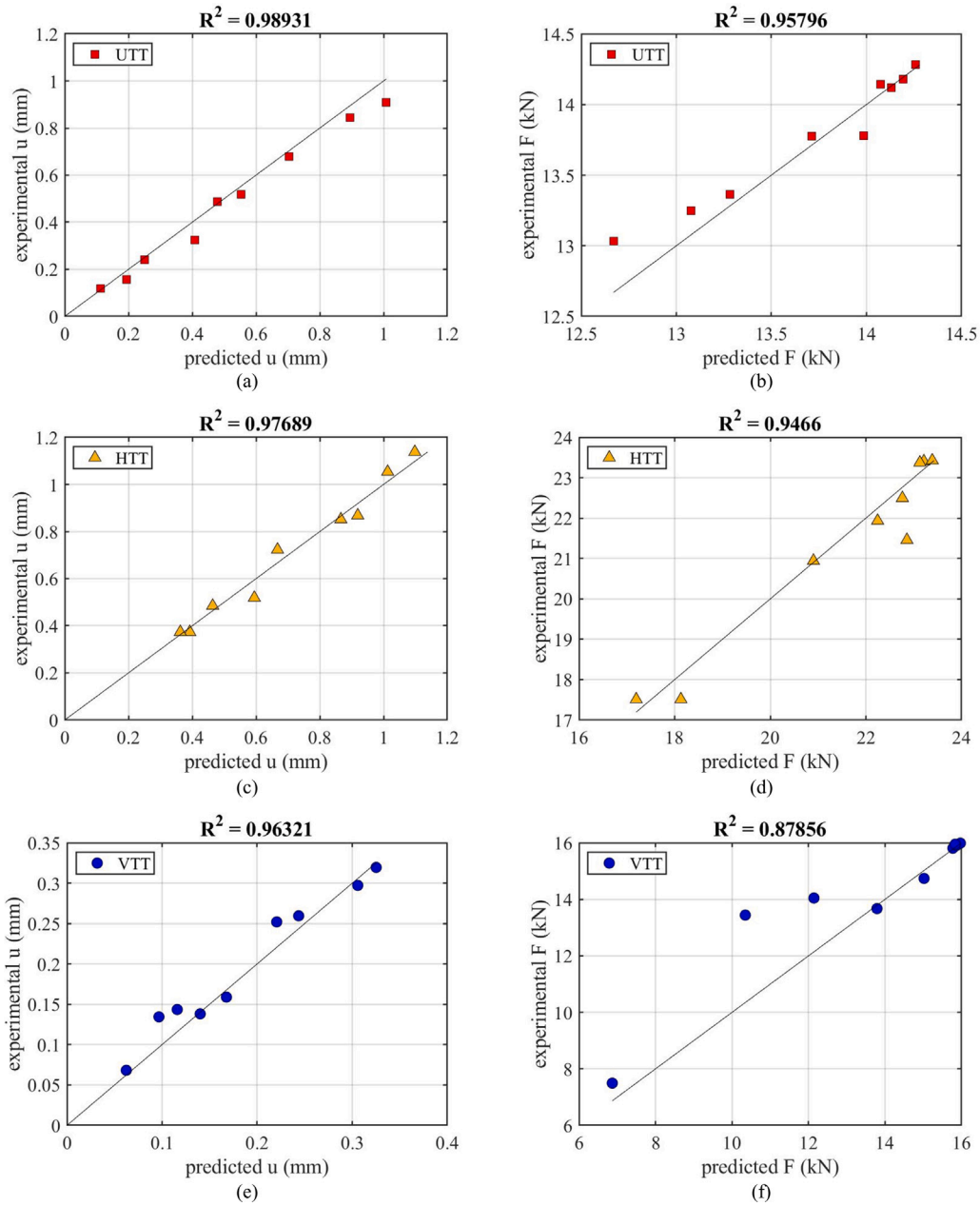
Fig. 18. Predicted vs. experimental force (*F*) and displacement (*u*), at fracture nucleation.
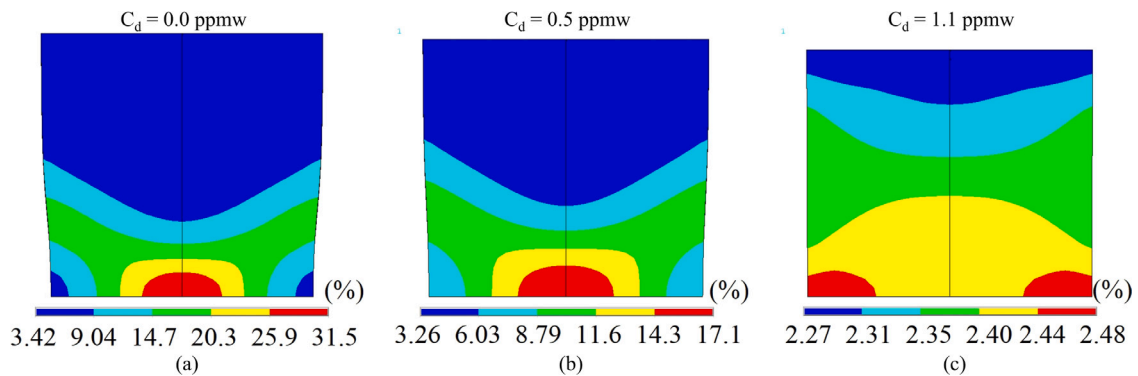

Fig. 19. Contour plot at fracture initiation of the first principal strain on the half-thickness plane for the un-notched tensile tests for diffusible H concentration (*C*$_d$) values ranging from 0.0 to 1.1 ppmw. (For interpretation of the references to colour in this figure legend, the reader is referred to the web version of this article.)
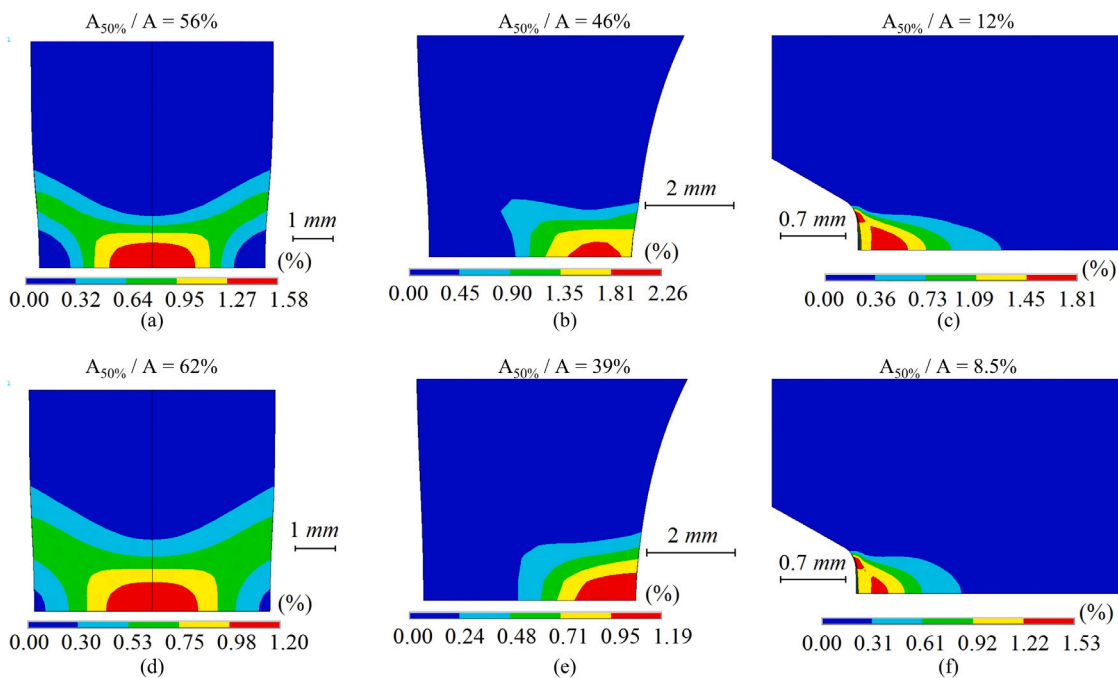
Fig. 20. Contour plot at fracture initiation of the void volume fraction for the un-notched (a,d), holed (b,e) and V-notched (c,f) specimens for diffusible H concentration (C_d) values of 0.0 and 0.5 ppmw. The plot is on the half-thickness plane. To numerically evaluate the "void volume concentration", the percentage of the ligament area $A_{50\%}/A$ in which the void volume fraction is at least 50% of the maximum value is reported for each specimen and condition. For the sake of clarity, the contour plots of the un-notched specimen were mirrored along its longitudinal axis. (For interpretation of the references to colour in this figure legend, the reader is referred to the web version of this article.)
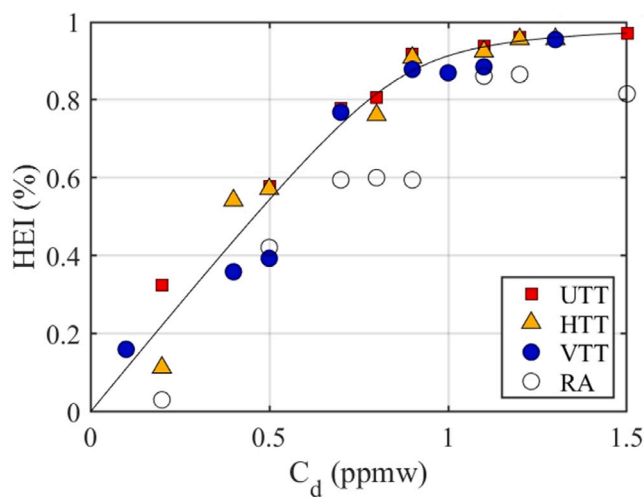

Fig. 21. Comparison between the HEI calculated from the first principal strain at fracture ε_f (full, coloured markers) and from the percentage reduction in area RA (hollow, black circles). The solid black line is the HEI calculated from Eq. (6).

Strain at fracture nucleation ε_f is the quantity controlling the onset of final fracture observed in the experimental tests. Accordingly, it is reasonable to adopt this quantity in order to define a more general HEI.

Fig. 21 shows the HEI calculated by choosing $\phi_f = \varepsilon_f$ for all the three testing conditions, compared with the HEI calculated from the reduction in area, RA, in UTTs. They show a similar trend but with significant differences. The HEI calculated from RA underestimates the value calculated from ε_f in the entire C_d range examined. There is also more scattering. These issues may be due to the greater difficulty in determining the fracture area of the tensile specimen. Fracture surfaces are often not flat, and significant differences between the actual and projected fracture surface of the specimen can occur. In addition, if the material is severely embrittled, the area contraction is small and

difficult to measure. The HEI identified through the first principal strain at fracture was found to be more conservative and more precise, and was consistent throughout the three tests. The critical H concentration, defined according to this HEI and to the 30% criterion, was about 0.3 ppmw.

With $C_d \leq 0.9$ ppmw the HEI follows a linear increasing trend. Above this threshold, most of the material ductility is lost.

The proposed procedure to evaluate the HEI is summarized in the following points:

- standard tensile SSRT with the as-received material is adopted
- standard tensile testing under H charged conditions with subsequent H content measurement is necessary
- the elastoplastic $\sigma - \varepsilon$ curve from the as-received test has to be obtained
- employing an optimization approach, the parameters of a damage model and a fracture criterion (based upon critical ε_1) are deduced from the experimental results.

This process requires the implementation and the solution of a nonlinear FE analysis, with an appropriate damage model. However, for the tested material, plastic damage does not seem to significantly influence the material response when severely notched specimens are involved. As a consequence, V-notched testing could be selected to assess the HEI based upon principal strain at fracture. In this case, no prior evaluation of a damage model is necessary. The results indicate that for low concentrations of H, when the material retains sufficient ductility to be of industrial use, the strain at fracture exhibits a reasonably linear dependence on the H concentration. As a consequence, a limited number of tests are needed to obtain preliminary data on the trend of the HEI dependence on H concentration.

6. Conclusions

This paper discusses H embrittlement in MS-AHSS and attempts to identify a mechanical property that can correctly represent the material degradation determined by H in different conditions (e.g. notches of

different severities), due to internal hydrogen. The following main conclusions can be drawn:

1. For the tested MS-AHSS grade, in agreement with other works, H reduces the ductility without significant loss of tensile strength. Thus a strain-based approach to the HEI can be used.
2. A material model, consisting of a constitutive $\sigma - \varepsilon$ law and damage model that was set-up using standard (un-notched) tensile tests, is suitable to identify the parameters by which the behaviour of notched specimens can be accurately reproduced by a common FE model up to failure.
3. The same material model is able to reproduce the behaviour of H-charged specimens of all tests, by assuming that H promotes the onset of plastic damage by influencing a parameter of Gursons damage model.
4. Local maximum principal strain data, obtained from FEM, at the experimentally observed failure is related to the measured average H concentration by an unique relationship despite the different notch severity.
5. The HEI defined by the local maximum principal strain at failure seems an accurate and useful approach by which a geometry-independent description of HE in sheet metal can be obtained (provided the material exhibits a similar HE behaviour in the standard qualification tests and a comparably slow hydrogen egress). Additionally, this approach was found to be more conservative and accurate than the method based on the reduction of area.
6. The proposed procedure to estimate the HEI requires: tensile testing of H-free un-notched specimens along with severely notched specimens tested in both H-free and H-charged conditions.
7. A HEI definition that is more conservative and less affected by the presence and severity of notches allows for a better management of quality assessment, material comparisons, HE risk evaluation and the design of structural components.

Declaration of competing interest

The authors declare that they have no known competing financial interests or personal relationships that could have appeared to influence the work reported in this paper.

Data availability

Data will be made available on request.

Acknowledgements

References

[1] N. Fonstein, Advanced High Strength Sheet Steels, Springer, 2015, http://dx.doi.org/10.1007/978-3-319-19165-2.

[2] S.K. Dwivedi, M. Vishwakarma, Effect of hydrogen in advanced high strength steel materials, Int. J. Hydrogen Energy 44 (51) (2019) 28007–28030, http://dx.doi.org/10.1016/j.ijhydene.2019.08.149.

[3] O. Kwon, K.Y. Lee, G.S. Kim, K.G. Chin, New trends in advanced high strength steel developments for automotive application, in: Materials Sciencme Forum, Vol. 638, Trans Tech Publ, 2010, pp. 136–141.

[4] J. Galán, L. Samek, P. Verleysen, K. Verbeken, Y. Houbaert, Advanced high strength steels for automotive industry, Rev. Metal. 48 (2) (2012) 118, http://dx.doi.org/10.3989/revmetalm.1158.

[5] R. Kuziak, R. Kawalla, S. Waengler, Advanced high strength steels for automotive industry, Arch. Civ. Mech. Eng. 8 (2) (2008) 103–117, http://dx.doi.org/10.1016/S1644-9665(12)60197-6.

[6] N. Baluch, Z.M. Udin, C.S. Abdullah, Advanced high strength steel in auto industry: an overview, Eng. Technol. Appl. Sci. Res. 4 (4) (2014) 686–689, http://dx.doi.org/10.48084/etasr.444.

[7] D.K. Matlock, J.G. Speer, E. De Moor, P.J. Gibbs, Recent developments in advanced high strength sheet steels for automotive applications: an overview, Jestech 15 (1) (2012) 1–12.

[8] J. Van Slycken, P. Verleysen, J. Degrieck, J. Bouquerel, B. De Cooman, Crashworthiness characterization and modelling of high-strength steels for automotive applications, Proc. Inst. Mech. Eng. D 220 (4) (2006) 391–400, http://dx.doi.org/10.1243/09544070JAUTO26.

[9] J.R. Shaw, B.K. Zuidema, New high strength steels help automakers reach future goals for safety, affordability, fuel efficiency and environmental responsibility, SAE Trans. (2001) 976–983, http://dx.doi.org/10.4271/2001-01-3041.

[10] L. Chao, W. Lei, L. Yang, Development of advanced high-strength steel used for automobile and its application in body design, Spec. Steel Technol. 2 (2012).

[11] M. Ma, H. Yi, Lightweight car body and application of high strength steels, in: Advanced Steels, Springer, 2011, pp. 187–198, http://dx.doi.org/10.1007/978-3-642-17665-4_20.

[12] J. Venezuela, Q. Liu, M. Zhang, Q. Zhou, A. Atrens, A review of hydrogen embrittlement of martensitic advanced high-strength steels, Corros. Rev. 34 (3) (2016) 153–186, http://dx.doi.org/10.1515/corrrev-2016-0006.

[13] H. Mohrbacher, Martensitic automotive steel sheet-fundamentals and metallurgical optimization strategies, in: Advanced Materials Research, Vol. 1063, Trans Tech Publ, 2015, pp. 130–142, http://dx.doi.org/10.4028/www.scientific.net/AMR.1063.130.

[14] V.H.L. Cortéz, F.A.R. Valdés, L.T. Treviño, Weldability of martensitic steel by resistance spot welding a neural network optimization in the automotive industry, Mater. Manuf. Process. 24 (12) (2009) 1412–1417, http://dx.doi.org/10.1080/10426910903343916.

[15] O. Bouaziz, H. Zurob, M. Huang, Driving force and logic of development of advanced high strength steels for automotive applications, Steel Res. Int. 84 (10) (2013) 937–947, http://dx.doi.org/10.1002/srin.201200288.

[16] J. Venezuela, Q. Liu, M. Zhang, Q. Zhou, A. Atrens, The influence of hydrogen on the mechanical and fracture properties of some martensitic advanced high strength steels studied using the linearly increasing stress test, Corros. Sci. 99 (2015) 98–117, http://dx.doi.org/10.1016/j.corsci.2015.06.038.

[17] G. Lovicu, M. Bottazzi, F. D'aiuto, M. De Sanctis, A. Dimatteo, C. Santus, R. Valentini, Hydrogen embrittlement of automotive advanced high-strength steels, Metall. Mater. Trans. A 43 (11) (2012) 4075–4087, http://dx.doi.org/10.1007/s11661-012-1280-8.

[18] Q. Liu, A. Atrens, A critical review of the influence of hydrogen on the mechanical properties of medium-strength steels, Corros. Rev. 31 (3–6) (2013) 85–103, http://dx.doi.org/10.1515/corrrev-2013-0023.

[19] S. Ramamurthy, A. Atrens, Stress corrosion cracking of high-strength steels, Corros. Rev. 31 (1) (2013) 1–31, http://dx.doi.org/10.1515/corrrev-2012-0018.

[20] J.A. Ronevich, J.G. Speer, D.K. Matlock, Hydrogen embrittlement of commercially produced advanced high strength sheet steels, SAE Int. J. Mater. Manuf. 3 (1) (2010) 255–267, http://dx.doi.org/10.4271/2010-01-0447.

[21] M. Nagumo, Fundamentals of Hydrogen Embrittlement, Vol. 921, Springer, 2016, http://dx.doi.org/10.1007/978-981-10-0161-1.

[22] J. Venezuela, F.Y. Lim, L. Liu, S. James, Q. Zhou, R. Knibbe, M. Zhang, H. Li, F. Dong, M.S. Dargusch, et al., Hydrogen embrittlement of an automotive 1700 MPa martensitic advanced high-strength steel, Corros. Sci. (2020) 108726, http://dx.doi.org/10.1016/j.corsci.2020.108726.

[23] C. Willan, Hydrogen embrittlement a historical overview, 2014.

[24] S. Lynch, Hydrogen embrittlement phenomena and mechanisms, Corros. Rev. 30 (3–4) (2012) 105–123, http://dx.doi.org/10.1515/corrrev-2012-0502.

[25] S. Ramamurthy, W. Lau, A. Atrens, Influence of the applied stress rate on the stress corrosion cracking of 4340 and 3.5NiCrMoV steels under conditions of cathodic hydrogen charging, Corros. Sci. 53 (7) (2011) 2419–2429, http://dx.doi.org/10.1016/j.corsci.2011.03.028.

[26] E. Martínez-Pañeda, Z.D. Harris, S. Fuentes-Alonso, J.R. Scully, J.T. Burns, On the suitability of slow strain rate tensile testing for assessing hydrogen embrittlement susceptibility, Corros. Sci. 163 (2020) 108291, http://dx.doi.org/10.1016/j.corsci.2019.108291.

[27] G. Pressouyre, F.M. Faure, Quantitative analysis of critical concentrations for hydrogen-induced cracking, in: Hydrogen Embrittlement: Prevention and Control, ASTM STP 962, American Society for Testing and Materials, 1988, pp. 353–371, http://dx.doi.org/10.1520/STP45314S.

[28] Q. Liu, Q. Zhou, J. Venezuela, M. Zhang, A. Atrens, Evaluation of the influence of hydrogen on some commercial DP, Q&P and TWIP advanced high-strength steels during automobile service, Eng. Fail. Anal. 94 (2018) 249–273, http://dx.doi.org/10.1016/j.engfailanal.2018.08.011.

[29] W. Wang, M. Li, C. He, X. Wei, D. Wang, H. Du, Experimental study on high strain rate behavior of high strength 600–1000 MPa dual phase steels and 1200 MPa fully martensitic steels, Mater. Des. 47 (2013) 510–521, http://dx.doi.org/10.1016/j.matdes.2012.12.068.

[30] E. Martínez-Pañeda, S. del Busto, C.F. Niordson, C. Betegón, Strain gradient plasticity modeling of hydrogen diffusion to the crack tip, Int. J. Hydrogen Energy 41 (24) (2016) 10265–10274, http://dx.doi.org/10.1016/j.ijhydene.2016.05.014.

[31] J.S. Kim, Y.H. Lee, D.L. Lee, K.-T. Park, C.S. Lee, Microstructural influences on hydrogen delayed fracture of high strength steels, Mater. Sci. Eng. A 505 (1–2) (2009) 105–110, http://dx.doi.org/10.1016/j.msea.2008.11.040.

[32] ISO Central Secretary, Steel – Measurement Method for the Evaluation of Hydrogen Embrittlement Resistance of High Strength Steels – Part 1: Constant Load Test, Standard ISO 16573-1:2020, International Organization for Standardization, Geneva, CH, 2020.

[33] R. Valentini, M.M. Tedesco, S. Corsinovi, L. Bacchi, M. Villa, Investigation of mechanical tests for hydrogen embrittlement in automotive PHS steels, Metals 9 (9) (2019) 934, http://dx.doi.org/10.3390/met9090934.

[34] K.-i. Mori, Y. Abe, K. Sedoguchi, Delayed fracture in cold blanking of ultra-high strength steel sheets, CIRP Ann. 68 (1) (2019) 297–300, http://dx.doi.org/10.1016/j.cirp.2019.04.111.

[35] D. Rudomilova, T. Prošek, G. Luckeneder, Techniques for investigation of hydrogen embrittlement of advanced high strength steels, Corros. Rev. 36 (5) (2018) 413–434, http://dx.doi.org/10.1515/corrrev-2017-0106.

[36] M. Loidl, O. Kolk, S. Veith, T. Göbel, Characterization of hydrogen embrittlement in automotive advanced high strength steels, Mater.wiss. Werkst.tech. 42 (12) (2011) 1105–1110, http://dx.doi.org/10.1002/mawe.201100917.

[37] D.P. Escobar, C. Miñambres, L. Duprez, K. Verbeken, M. Verhaege, Internal and surface damage of multiphase steels and pure iron after electrochemical hydrogen charging, Corros. Sci. 53 (10) (2011) 3166–3176, http://dx.doi.org/10.1016/j.corsci.2011.05.060.

[38] T. Depover, D.P. Escobar, E. Wallaert, Z. Zermout, K. Verbeken, Effect of hydrogen charging on the mechanical properties of advanced high strength steels, Int. J. Hydrogen Energy 39 (9) (2014) 4647–4656, http://dx.doi.org/10.1016/j.ijhydene.2013.12.190.

[39] M.L. Martin, M. Dadfarnia, A. Nagao, S. Wang, P. Sofronis, Enumeration of the hydrogen-enhanced localized plasticity mechanism for hydrogen embrittlement in structural materials, Acta Mater. 165 (2019) 734–750, http://dx.doi.org/10.1016/j.actamat.2018.12.014.

[40] M. Wang, E. Akiyama, K. Tsuzaki, Effect of hydrogen on the fracture behavior of high strength steel during slow strain rate test, Corros. Sci. 49 (11) (2007) 4081–4097, http://dx.doi.org/10.1016/j.corsci.2007.03.038.

[41] VDEh, Test of the Resistance of Advanced High Strength Steels (AHSS) for Automotive Applications Against Production Related Hydrogen Induced Brittle Fracture, Standard SEP1970:2011, Verlag Stahleisen GmbH, Düsseldorf, Germany, 2011.

[42] Standard Practice for Slow Strain Rate Testing to Evaluate the Susceptibility of Metallic Materials to Environmentally Assisted Cracking, Standard ASTM G129-00(2013), ASTM International, West Conshohocken, PA, 2013.

[43] L. Peral, A. Zafra, J. Belzunce, C. Rodríguez, Effects of hydrogen on the fracture toughness of CrMo and CrMoV steels quenched and tempered at different temperatures, Int. J. Hydrogen Energy 44 (7) (2019) 3953–3965, http://dx.doi.org/10.1016/j.ijhydene.2018.12.084.

[44] Y. Ogawa, S. Okazaki, O. Takakuwa, H. Matsunaga, The roles of internal and external hydrogen in the deformation and fracture processes at the fatigue crack tip zone of metastable austenitic stainless steels, Scr. Mater. 157 (2018) 95–99, http://dx.doi.org/10.1016/j.scriptamat.2018.08.003.

[45] C. Zhang, W. Hui, X. Zhao, Y. Zhang, X. Zhao, Hydrogen-induced delayed fracture behaviour of V+Nb-microalloyed high-strength bolt steel with internal and environmental hydrogen, Corros. Sci. 209 (2022) 110710, http://dx.doi.org/10.1016/j.corsci.2022.110710.

[46] S. Shen, X. Song, Q. Li, X. Li, R. Zhu, G. Yang, Effect of Cr x C y–NiCr coating on the hydrogen embrittlement of 17-4 PH stainless steel using the smooth bar tensile test, J. Mater. Sci. 54 (9) (2019) 7356–7368, http://dx.doi.org/10.1007/s10853-019-03356-4.

[47] V. Colla, R. Valentini, Assessment of critical hydrogen concentration in as-cast and hot-rolled billets in medium carbon steels, Steel Res. Int. 91 (9) (2020) 2000126, http://dx.doi.org/10.1002/srin.202000126.

[48] C. Zhou, D. Tang, K. Zhang, F. Wu, P. Lin, Y. Jin, L. Zhang, J. Zheng, Effect of manganese content on the hydrogen embrittlement of twinning-induced plasticity (TWIP) steels under hydrogen charging and hydrogen environment, Mater. Sci. Eng. A 861 (2022) 144289, http://dx.doi.org/10.1016/j.msea.2022.144289.

[49] Z. Yang, Z. Liu, J. Liang, J. Su, Z. Yang, B. Zhang, G. Sheng, Correlation between the microstructure and hydrogen embrittlement resistance in a precipitation-hardened martensitic stainless steel, Corros. Sci. 182 (2021) 109260, http://dx.doi.org/10.1016/j.corsci.2021.109260.

[50] H. Fu, W. Wang, H. Zhao, F. Jin, J. Li, Study of hydrogen-induced delayed fracture in high-Mn TWIP/TRIP steels during in situ electrochemical hydrogen-charging: Role of microstructure and strain rate in crack initiation and propagation, Corros. Sci. 162 (2020) 108191, http://dx.doi.org/10.1016/j.corsci.2019.108191.

[51] L. Briottet, I. Moro, P. Lemoine, Quantifying the hydrogen embrittlement of pipeline steels for safety considerations, Int. J. Hydrogen Energy 37 (22) (2012) 17616–17623, http://dx.doi.org/10.1016/j.ijhydene.2012.05.143.

[52] S. Liu, W. Wu, H. Fu, J. Li, Equivalence in evaluating hydrogen-assisted fracture strength of slow strain rate tensile and constant load tensile for three precipitation-hardened martensitic stainless steels: Effect of large-sized particles, Corros. Sci. 215 (2023) 111050, http://dx.doi.org/10.1016/j.corsci.2023.111050.

[53] M. Wang, E. Akiyama, K. Tsuzaki, Determination of the critical hydrogen concentration for delayed fracture of high strength steel by constant load test and numerical calculation, Corros. Sci. 48 (8) (2006) 2189–2202, http://dx.doi.org/10.1016/j.corsci.2005.07.010.

[54] E. Fangnon, Y. Yagodzinskyy, E. Malictki, S. Mehtonen, E. Virolainen, P. Vilaça, Determination of critical hydrogen concentration and its effect on mechanical performance of 2200 MPa and 600 HBW martensitic ultra-high-strength steel, Metals 11 (6) (2021) http://dx.doi.org/10.3390/met11060984.

[55] H. Li, J. Venezuela, Q. Zhou, V. Luzin, M. Yan, Z. Shi, R. Knibbe, M. Zhang, F. Dong, M.S. Dargusch, A. Atrens, Hydrogen-induced delayed fracture of a 1180 MPa martensitic advanced high-strength steel under U-bend loading, Mater. Today Commun. 26 (2021) 101887, http://dx.doi.org/10.1016/j.mtcomm.2020.101887.

[56] J. Venezuela, T. Hill, Q. Zhou, H. Li, Z. Shi, F. Dong, R. Knibbe, M. Zhang, M.S. Dargusch, A. Atrens, Hydrogen-induced fast fracture in notched 1500 and 1700 MPa class automotive martensitic advanced high-strength steel, Corros. Sci. 188 (2021) 109550, http://dx.doi.org/10.1016/j.corsci.2021.109550.

[57] J. Venezuela, Q. Zhou, Q. Liu, H. Li, M. Zhang, M.S. Dargusch, A. Atrens, The influence of microstructure on the hydrogen embrittlement susceptibility of martensitic advanced high strength steels, Mater. Today Commun. 17 (2018) 1–14, http://dx.doi.org/10.1016/j.mtcomm.2018.07.011.

[58] H. Li, J. Venezuela, Z. Qian, Q. Zhou, Z. Shi, M. Yan, R. Knibbe, M. Zhang, F. Dong, A. Atrens, Hydrogen fracture maps for sheared-edge-controlled hydrogen-delayed fracture of 1180 MPa advanced high-strength steels, Corros. Sci. 184 (2021) 109360, http://dx.doi.org/10.1016/j.corsci.2021.109360.

[59] H. Li, J. Venezuela, Q. Zhou, Z. Shi, M. Yan, R. Knibbe, M. Zhang, F. Dong, A. Atrens, Effect of shearing prestrain on the hydrogen embrittlement of 1180 MPa grade martensitic advanced high-strength steel, Corros. Sci. 199 (2022) 110170, http://dx.doi.org/10.1016/j.corsci.2022.110170.

[60] V. Shubina, A. Nazarov, F. Vucko, N. Larché, D. Thierry, Effect of cathodic polarisation switch-off on the passivity and stability to crevice corrosion of AISI 304L stainless steel, Materials 14 (2021) 2921, http://dx.doi.org/10.3390/ma14112921.

[61] J. Crank, The Mathematics of Diffusion, Oxford University Press, 1979.

[62] T. Kannengiesser, N. Tiersch, Measurements of diffusible hydrogen contents at elevated temperatures using different hot extraction techniques—An international round robin test, Weld. World 54 (5–6) (2010) R115–R122, http://dx.doi.org/10.1007/BF03263497.

[63] J.-L. Lee, J.-Y. Lee, Hydrogen retrapping after thermal charging of hydrogen in iron single crystal, Metall. Trans. A 20 (9) (1989) 1793–1802, http://dx.doi.org/10.1007/BF02663210.

[64] A. Drexler, C. Bergmann, G. Manke, V. Kokotin, K. Mraczek, M. Pohl, W. Ecker, On the local evaluation of the hydrogen susceptibility of cold-formed and heat treated advanced high strength steel (AHSS) sheets, Mater. Sci. Eng. A 800 (2021) 140276, http://dx.doi.org/10.1016/j.msea.2020.140276.

[65] D. Guedes, L.C. Malheiros, A. Oudriss, S. Cohendoz, J. Bouhattate, J. Creus, F. Thébault, M. Piette, X. Feaugas, The role of plasticity and hydrogen flux in the fracture of a tempered martensitic steel: A new design of mechanical test until fracture to separate the influence of mobile from deeply trapped hydrogen, Acta Mater. 186 (2020) 133–148, http://dx.doi.org/10.1016/j.actamat.2019.12.045.

[66] A.J. Kumnick, H.H. Johnson, Hydrogen transport through annealed and deformed Armco Iron, Metall. Trans. 5 (5) (1974) 1199–1206, http://dx.doi.org/10.1007/bf02644334.

[67] A. Kumnick, H. Johnson, Deep trapping states for hydrogen in deformed iron, Acta Metall. 28 (1) (1980) 33–39, http://dx.doi.org/10.1016/0001-6160(80)90038-3.

[68] W.Y. Choo, J.Y. Lee, Effect of cold working on the hydrogen trapping phenomena in pure iron, Metall. Trans. A 14 (7) (1983) 1299–1305, http://dx.doi.org/10.1007/bf02664812.

[69] P. Sofronis, R. McMeeking, Numerical analysis of hydrogen transport near a blunting crack tip, J. Mech. Phys. Solids 37 (3) (1989) 317–350, http://dx.doi.org/10.1016/0022-5096(89)90002-1.

[70] A. Krom, R. Koers, A. Bakker, Hydrogen transport near a blunting crack tip, J. Mech. Phys. Solids 47 (4) (1999) 971–992, http://dx.doi.org/10.1016/S0022-5096(98)00064-7.

[71] B. Kan, W. Wu, Z. Yang, J. Li, Stress-induced hydrogen redistribution and corresponding fracture behavior of Q960E steel at different hydrogen content, Mater. Sci. Eng. A 775 (2020) 138963, http://dx.doi.org/10.1016/j.msea.2020.138963.

[72] A. Turnbull, D. Ferriss, H. Anzai, Modelling of the hydrogen distribution at a crack tip, Mater. Sci. Eng. A 206 (1) (1996) 1–13, http://dx.doi.org/10.1016/0921-5093(95)09897-6.

[73] T.-Y. Zhang, Y.-P. Zheng, Effects of absorption and desorption on hydrogen permeation—I. Theoretical modeling and room temperature verification, Acta Mater. 46 (14) (1998) 5023–5033, http://dx.doi.org/10.1016/S1359-6454(98)00176-1, URL https://www.sciencedirect.com/science/article/pii/S1359645498001761.

[74] Y.-P. Zheng, T.-Y. Zhang, Effects of absorption and desorption on hydrogen permeation—II. Experimental measurements of activation energies, Acta Mater. 46 (14) (1998) 5035–5043, http://dx.doi.org/10.1016/S1359-6454(98)00177-3, URL https://www.sciencedirect.com/science/article/pii/S1359645498001773.

[75] A. Turnbull, Perspectives on hydrogen uptake, diffusion and trapping, Int. J. Hydrogen Energy 40 (47) (2015) 16961–16970, http://dx.doi.org/10.1016/j.ijhydene.2015.06.147, Special issue on 1st International Conference on Hydrogen Storage, Embrittlement and Applications (Hy-SEA 2014), 26-30 October 2014, Rio de Janeiro, Brazil.

[76] C. Hurley, F. Martin, L. Marchetti, J. Chêne, C. Blanc, E. Andrieu, Numerical modeling of thermal desorption mass spectroscopy (TDS) for the study of hydrogen diffusion and trapping interactions in metals, Int. J. Hydrogen Energy 40 (8) (2015) 3402–3414, http://dx.doi.org/10.1016/j.ijhydene.2015.01.001.

[77] A. Díaz, J. Alegre, I. Cuesta, Coupled hydrogen diffusion simulation using a heat transfer analogy, Int. J. Mech. Sci. 115–116 (2016) 360–369, http://dx.doi.org/10.1016/j.ijmecsci.2016.07.020.

[78] Y. Charles, H. Nguyen, M. Gaspérini, FE simulation of the influence of plastic strain on hydrogen distribution during an U-bend test, Int. J. Mech. Sci. 120 (2017) 214–224, http://dx.doi.org/10.1016/j.ijmecsci.2016.11.017.

[79] A. Díaz, A. Zafra, E. Martínez-Pañeda, J. Alegre, J. Belzunce, I. Cuesta, Simulation of hydrogen permeation through pure iron for trapping and surface phenomena characterisation, Theor. Appl. Fract. Mech. 110 (2020) 102818, http://dx.doi.org/10.1016/j.tafmec.2020.102818.

[80] E. Martínez-Pañeda, A. Díaz, L. Wright, A. Turnbull, Generalised boundary conditions for hydrogen transport at crack tips, Corros. Sci. 173 (2020) 108698, http://dx.doi.org/10.1016/j.corsci.2020.108698, URL https://www.sciencedirect.com/science/article/pii/S0010938X20305345.

[81] A. Zafra, J. Belzunce, C. Rodríguez, I. Fernández-Pariente, Hydrogen embrittlement of the coarse grain heat affected zone of a quenched and tempered 42CrMo4 steel, Int. J. Hydrogen Energy 45 (33) (2020) 16890–16908, http://dx.doi.org/10.1016/j.ijhydene.2020.04.097.

[82] A. Zafra, Z. Harris, E. Korec, E. Martínez-Pañeda, On the relative efficacy of electropermeation and isothermal desorption approaches for measuring hydrogen diffusivity, Int. J. Hydrogen Energy 48 (3) (2023) 1218–1233, http://dx.doi.org/10.1016/j.ijhydene.2022.10.025.

[83] A. Zafra, G. Álvarez, G. Benoit, G. Henaff, E. Martinez-Pañeda, C. Rodríguez, J. Belzunce, Hydrogen-assisted fatigue crack growth: Pre-charging vs in-situ testing in gaseous environments, Mater. Sci. Eng. A 871 (2023) 144885, http://dx.doi.org/10.1016/j.msea.2023.144885.

[84] W. Rasband, ImageJ, U. S. National Institutes of Health, Bethesda, Maryland, USA, 1997-2018, URL https://imagej.nih.gov/ij/.

[85] J. Rehrl, K. Mraczek, A. Pichler, E. Werner, Mechanical properties and fracture behavior of hydrogen charged AHSS/UHSS grades at high-and low strain rate tests, Mater. Sci. Eng. A 590 (2014) 360–367, http://dx.doi.org/10.1016/j.msea.2013.10.044.

[86] M. Möser, V. Schmidt, Fractography and mechanism of hydrogen cracking - The fisheye concept, in: S. Valluri, D. Taplin, P.R. Rao, J. Knott, R. Dubey (Eds.), Fracture 84, Pergamon, 1984, pp. 2459–2466, http://dx.doi.org/10.1016/B978-1-4832-8440-8.50254-4.

[87] B. Strnadel, Failure of steels caused by hydrogen induced microcracking, Eng. Fract. Mech. 61 (3) (1998) 299–310, http://dx.doi.org/10.1016/S0013-7944(98)00073-3.

[88] E. Merson, A. Vinogradov, D. Merson, Application of acoustic emission method for investigation of hydrogen embrittlement mechanism in the low-carbon steel, J. Alloys Compd. 645 (2015) S460–S463, http://dx.doi.org/10.1016/j.jallcom.2014.12.083, Supplement Issue: Proceedings from the 14th International Symposium on Metal-Hydrogen Systems: Fundamentals and Applications, 2014 (MH2014).

[89] E. Merson, P. Myagkikh, V. Poluyanov, D. Merson, A. Vinogradov, Features of the hydrogen-assisted cracking mechanism in the low-carbon steel at ex- and in-situ hydrogen charging, Procedia Struct. Integr. 13 (2018) 1141–1147, http://dx.doi.org/10.1016/j.prostr.2018.12.238, ECF22 - Loading and Environmental effects on Structural Integrity.

[90] A. Nagao, M. Dadfarnia, B.P. Somerday, P. Sofronis, R.O. Ritchie, Hydrogen-enhanced-plasticity mediated decohesion for hydrogen-induced intergranular and "quasi-cleavage" fracture of lath martensitic steels, J. Mech. Phys. Solids 112 (2018) 403–430, http://dx.doi.org/10.1016/j.jmps.2017.12.016.

[91] Q. Liu, Q. Zhou, J. Venezuela, M. Zhang, A. Atrens, The role of the microstructure on the influence of hydrogen on some advanced high-strength steels, Mater. Sci. Eng. A 715 (2018) 370–378, http://dx.doi.org/10.1016/j.msea.2017.12.079.

[92] S. Zhu, C. Zhang, Z. Yang, C. Wang, Hydrogen's influence on reduced activation ferritic/martensitic steels' elastic properties: density functional theory combined with experiment, Nucl. Eng. Technol. 49 (8) (2017) 1748–1751, http://dx.doi.org/10.1016/j.net.2017.08.021.

[93] P. Sofronis, Y. Liang, N. Aravas, Hydrogen induced shear localization of the plastic flow in metals and alloys, Eur. J. Mech. A Solids 20 (6) (2001) 857–872, http://dx.doi.org/10.1016/S0997-7538(01)01179-2.

[94] S. Huang, Y. Zhang, C. Yang, H. Hu, Fracture strain model for hydrogen embrittlement based on hydrogen enhanced localized plasticity mechanism, Int. J. Hydrogen Energy 45 (46) (2020) 25541–25554, http://dx.doi.org/10.1016/j.ijhydene.2020.06.271.

[95] V.K. Barnwal, S.-Y. Lee, J.-H. Kim, F. Barlat, Failure characteristics of advanced high strength steels at macro and micro scales, Mater. Sci. Eng. A 754 (2019) 411–427, http://dx.doi.org/10.1016/j.msea.2019.03.087.

[96] C. Zhang, Y. Wang, Z. Chen, N. Yang, Y. Lou, T. Clausmeyer, A.E. Tekkaya, Q. Zhang, Characterization of plasticity and fracture of an QP1180 steel sheet, Procedia Manuf. 50 (2020) 529–534, http://dx.doi.org/10.1016/j.promfg.2020.08.095, 18th International Conference on Metal Forming 2020.

[97] Z. Yao, W. Wang, Full-range strain-hardening behavior of structural steels: Experimental identification and numerical simulation, J. Construct. Steel Res. 194 (2022) 107329, http://dx.doi.org/10.1016/j.jcsr.2022.107329.

[98] A.L. Gurson, Continuum theory of ductile rupture by void nucleation and growth: Part I—Yield criteria and flow rules for porous ductile media, J. Eng. Mater. Technol. 99 (1) (1977) 2–15, http://dx.doi.org/10.1115/1.3443401.

[99] H.G. Wilsdorf, Void initiation, growth, and coalescence in ductile fracture of metals, J. Electron. Mater. 4 (5) (1975) 791–809.

[100] H. Yu, J.S. Olsen, A. Alvaro, L. Qiao, J. He, Z. Zhang, Hydrogen informed Gurson model for hydrogen embrittlement simulation, Eng. Fract. Mech. 217 (2019) 106542, http://dx.doi.org/10.1016/j.engfracmech.2019.106542.

[101] R. Depraetere, W. De Waele, S. Hertelé, Fully-coupled continuum damage model for simulation of plasticity dominated hydrogen embrittlement mechanisms, Comput. Mater. Sci. 200 (2021) 110857, http://dx.doi.org/10.1016/j.commatsci.2021.110857.

[102] M. Lin, H. Yu, Y. Ding, V. Olden, A. Alvaro, J. He, Z. Zhang, Simulation of ductile-to-brittle transition combining complete Gurson model and CZM with application to hydrogen embrittlement, Eng. Fract. Mech. 268 (2022) 108511, http://dx.doi.org/10.1016/j.engfracmech.2022.108511.

[103] M. Lin, H. Yu, Y. Ding, G. Wang, V. Olden, A. Alvaro, J. He, Z. Zhang, A predictive model unifying hydrogen enhanced plasticity and decohesion, Scr. Mater. 215 (2022) 114707, http://dx.doi.org/10.1016/j.scriptamat.2022.114707.

[104] A. Díaz, J. Alegre, I. Cuesta, Z. Zhang, Numerical study of hydrogen influence on void growth at low triaxialities considering transient effects, Int. J. Mech. Sci. 164 (2019) 105176, http://dx.doi.org/10.1016/j.ijmecsci.2019.105176.

[105] V. Tvergaard, Influence of void nucleation on ductile shear fracture at a free surface, J. Mech. Phys. Solids 30 (6) (1982) 399–425.

[106] T. Haruna, T. Shibata, Initiation and growth of stress corrosion cracks in type 316L stainless steel during slow strain rate testing, Corrosion 50 (10) (1994) arXiv:https://onepetro.org/corrosion/article-pdf/2184164/nace-94100785.pdf.

[107] T. Wierzbicki, Y. Bao, Y.-W. Lee, Y. Bai, Calibration and evaluation of seven fracture models, Int. J. Mech. Sci. 47 (4–5) (2005) 719–743.

[108] N.-H. Kim, C.-S. Oh, Y.-J. Kim, K.-B. Yoon, Y.-W. Ma, Hydrogen-assisted stress corrosion cracking simulation using the stress-modified fracture strain model, J. Mech. Sci. Technol. 26 (8) (2012) 2631–2638, http://dx.doi.org/10.1007/s12206-012-0642-x.

[109] G.-G. Youn, Y.-J. Kim, J.-S. Kim, P.-S. Lam, A fracture strain based numerical prediction method for hydrogen effect on fracture toughness, Int. J. Mech. Sci. 202–203 (2021) 106492, http://dx.doi.org/10.1016/j.ijmecsci.2021.106492.

[110] S. Huang, S. Hui, Predictive environmental hydrogen embrittlement on fracture toughness of commercial ferritic steels with hydrogen-modified fracture strain model, Int. J. Hydrogen Energy 47 (19) (2022) 10777–10787, http://dx.doi.org/10.1016/j.ijhydene.2021.12.128.